Aerodynamics of a Transonic Turbine Vane with a 3D Contoured Endwall, Upstream Purge Flow, and a Backward-Facing Step

John Gillespie

Thesis submitted to the faculty of the
Virginia Polytechnic Institute and State University
in partial fulfillment of the requirements for the degree of

Master of Science
in
Aerospace Engineering

Todd Lowe, Co-Chair
Wing F. Ng, Co-Chair
Lin Ma

July 30,2017
Blacksburg, VA

Keywords: Vane, 3D Endwall Contour, Backward-Facing Step, Purge Flow, Turbine

WARNING - This document contains technical data whose export is restricted by the Export Administration Act of 1979, as amended, Title 50, U.S.C., App. 2401 et seq. Violations of these export laws are subject to severe criminal penalties. This document contains proprietary information owned by Honeywell Aerospace restricted by Export Control Classification Number 9E991.

Aerodynamics of a Transonic Turbine Vane with a 3D Contoured Endwall, Upstream Purge Flow, and a Backward-Facing Step

John Gillespie

Abstract

This experiment investigated the effects of a non-axisymmetric endwall contour and upstream purge flow on the secondary flow of an inlet guide vane. Three cases were tested in a transonic wind tunnel with an exit Mach number of 0.93-a flat endwall with no upstream purge flow, the same flat endwall with upstream purge flow, and a 3D contoured endwall with upstream purge flow. All cases had a backward-facing step upstream of the vanes. Five-hole probe measurements were taken 0.2, 0.4, and 0.6 Cx downstream of the vane row trailing edge, and were used to calculate loss coefficient, secondary velocity, and secondary kinetic energy. Additionally, surface static pressure measurements were taken to determine the vane loading at 4% spanwise position. Surface oil flow visualizations were performed to analyze the flow qualitatively. No statistically significant differences were found between the three cases in mass averaged downstream measurements. The contoured endwall redistributed losses, rather than making an improvement distinguishable beyond experimental uncertainty. Flow visualization found that the passage vortex penetrated further in the spanwise direction into the passage for the contoured endwall (compared to the flat endwall), and stayed closer to the endwall with a blowing ratio of 1.5 with a flat endwall (compared to no blowing with flat endwall). This was corroborated by the five hole probe results.

Aerodynamics of a Transonic Turbine Vane with a 3D Contoured Endwall, Upstream Purge Flow, and a Backward-Facing Step

John Gillespie

General Audience Abstract

This experiment investigated effects of a specially designed endwall (the wall of a jet engine where the vanes end) and adding extra flow upstream through a slot on the inefficiencies of a jet engine vane (a stationary part of the engine that looks like a wing). Three cases were tested in a high-speed wind tunnel at almost the speed of sound-a flat endwall with no extra flow upstream, the same flat endwall with extra flow upstream, and the specially designed endwall with extra flow upstream. All cases had a backward-facing step (a step in the direction as if you are walking downstairs) upstream of the vanes. Measurements of flow direction and pressure were taken at three locations close to the vanes, and were used to calculate parameters relating to efficiency. Additionally, measurements were taken to verify that the vanes functioned correctly. Different colored paints (that do not stick) were used to see how the flow changed between each case. Measurements showed there were no major differences in overall efficiency between the three cases. The specially designed endwall made some areas more efficient, and others less efficient, rather than making the overall vane more efficient. The colored paints showed that a region of spinning flow went further away from the wall with the specially designed endwall. The paints also found that the same region of spinning flow stayed closer to wall when extra flow was added upstream. This was corroborated by the five hole probe results. The results from the paints agreed with the measurements of flow direction and pressure. In conclusion, neither the specially designed endwall or the extra flow made much difference in the overall efficiency (instead, they made some parts more efficient and other parts less efficient).

Acknowledgements

I would like to thank the many people who contributed to this project in various ways. Without their assistance, this project would not have been possible.

As advisors, Dr. Wing Ng and Dr. Todd Lowe provided valuable oversight to the project, as well as lending their expertise in solving the problems that came up over the course of completing the project.

Dr. Bao Nguyen continually met with us over the course of the project, and represented Honeywell in our meetings. His work to set up the project was vitally important; without it there would not have been any project. He provided the endwall geometry to be tested, as well as performing CFD to predict its behavior. He made sure we kept the project on track for completion and helped to decide what should be tested.

Marcie Stuber assisted in performing tests with the wind tunnel, as well as doing some PIV (Particle Image Velocimetry) setup and testing.

Dan Cadel developed PIV testing for this cascade. Though he was only involved in the preliminary testing for this project, and we did not end up using PIV results, his advice on fluid behavior and support during getting the cascade running was very helpful.

Dominic Agentis and John Hutchinson worked on this project as senior undergrads during the design phase of the project. Dominic did preliminary PIV setup, and John designed the traverse box that was used to collect 5-hole probe data.

Kevin Peterson preceded me at the lab, and taught me how to operate the tunnel. He also provided advice during the design phase of the project. He and Sean Brennan helped troubleshoot problems that came up early on in testing.

Other members of the lab who were not directly on the project, but provided useful advice, included David Mayo, Alan Arisi, Andrew Boulanger, and Chu Kim.

The members of the Virginia Tech ME machine shop- Bill Songer, Phillip Long, Timothy Kessinger, and Johnny Cox, did most of the machining needed for the project. Matt Mills from the AOE machine shop ran the 3D printer to create the airfoils and endwalls.

I would also like to thank Honeywell Aerospace for sponsoring the project, and the many people who helped make this research project possible.

Table of Contents

1 Introduction 1

2 Literature Review 3

3 Experimental Setup 5

  3.1 Virginia Tech Transonic Wind Tunnel 5

  3.2 Test Section Details 5

  3.3 Vane and Endwall Details 8

  3.4 Upstream Purge Flow 9

  3.5 Test Configurations 10

4 Results and Discussion 10

  4.1 Vane Loading 10

  4.2 Flow Visualizations 14

  4.3 Downstream Measurements 16

    4.3.1 Local Loss Coefficient 18

    4.3.2 Overall Loss Coefficient 23

    4.3.3 Secondary Velocity 23

    4.3.4 Secondary Kinetic Energy 27

5 Conclusions 33

6 Recommendations for Future Work 33

7 References 34

Appendix 36

  A General Tunnel Instrumentation 36

    A.1 Upstream Total and Static Pressure Measurements 36

    A.2 Downstream Static Measurements 36

  B Additional Vane and Endwall Details 36

  C Additional Purge Flow Details 38

  D Traverse Setup Details 40

  E Five-hole Probe Details 40

  F Repeatability 42

  G Uncertainty Analysis 42

  H Leakage Discussion 46

List of Figures

Figure 1. Virginia Tech's Transonic Wind Tunnel 5
Figure 2. Side view of linear cascade with the window removed and no side wall 6
Figure 3. Side view of the test section. Measured passages can be seen through the transparent window. 7
Figure 4. Upstream geometry schematic. 7
Figure 5. Linear cascade with window removed. Lower tailboard is not present in the picture. 8
Figure 6. Tests were performed with a flat endwall (Top) and contoured endwall (Bottom) 8
Figure 7. Location of loading measurement locations. 10
Figure 8 Loading data, 50% span, Flat Endwall without Blowing 11
Figure 9. Loading for the flat endwall case without blowing at 4% span 12
Figure 10. Loading for the flat endwall case with a blowing ratio of 1.5 at 4% span 12
Figure 11. Blade loading data for contoured endwall test configuration at 4% span 13
Figure 12 Loading comparison between flat and contoured endwalls with a blowing ratio of 1.5 13
Figure 13. Before (Left) and after (Right) pictures for flow visualization tests. 14
Figure 14. Features measured in flow visualization (view of pressure side) 15
Figure 15. Features measured in flow visualization (view of suction side) 16
Figure 16. Probe measurement locations 17
Figure 17. Local loss coefficient for flat endwall with blowing (Left) and flat endwall without blowing (Right) at 0.2 Cx (Top), 0.4 Cx (Middle), and 0.6 Cx (Bottom) 19
Figure 18. Local loss coefficient for flat endwall with blowing (Left) and contoured endwall with blowing (Right) at 0.2 Cx (Top), 0.4 Cx (Middle), and 0.6 Cx (Bottom) 20
Figure 19. Comparison between flat and contoured endwall cases for mass averaged loss coefficient for each spanwise position 21
Figure 20. Comparison between blowing and no blowing for mass averaged loss coefficient for each spanwise position 22
Figure 21. Secondary velocity magnitude for flat endwall (Left) and contoured endwall (Right) at 0.2 Cx (Top), 0.4 Cx (Middle), and, 0.6 Cx (Bottom) 25
Figure 22. Secondary velocity magnitude for flat endwall (Left) and contoured endwall (Right) at 0.2 Cx (Top), 0.4 Cx (Middle), and, 0.6 Cx (Bottom) 26
Figure 23. Secondary kinetic energy for flat endwall (Left) and contoured endwall (Right) at 0.2 Cx (Top), 0.4 Cx (Middle), and, 0.6 Cx (Bottom) 29
Figure 24. Secondary kinetic energy for flat endwall (Left) and contoured endwall (Right) at 0.2 Cx (Top), 0.4 Cx (Middle), and, 0.6 Cx (Bottom) 30
Figure 25. Mass averaged SKE plots for contoured and flat endwalls at 0.2 Cx (Top), 0.4 Cx (Middle), and 0.6 Cx (Bottom) 31
Figure 26. Mass averaged SKE plots for flat endwall with BR=0 and BR=1.5 at 0.2 Cx (Top), 0.4 Cx (Middle), and 0.6 Cx (Bottom) 32
Figure 27. Flat endwall configuration as three pieces. Central piece has removable vanes 37

Figure 28. Contoured endwall. Vanes are bolted individually to each of the cutouts in the endwall 37
Figure 29. View of external plenum. Cooling supplied to both sides simultaneously 38
Figure 30. Flow of purge flow air through the plenum and into the test section 39
Figure 31. Smooth interface between window and endwall 40
Figure 32. Five-hole probe dimensions 41
Figure 33. Five-hole probe data collected on two separate days (same test setup and spanwise location) 42
Figure 34. Verification that there is no leakage underneath the vane (underside of vane is also checked …….41

List of Tables

Table 1. Test configurations for the experiment 10
Table 2. Qualitative comparison of flow visualizations from flat and contoured endwalls 16
Table 3. Mass averaged loss coefficient for each case 23
Table 4. Total mass averaged SKE for each case. 28

Nomenclature

M_{isen}	Isentropic Mach number
Ps_{surf}	Static pressure at the surface of a vane
Pt_{in}	Total pressure at the inlet of the tunnel
γ	Specific heat ratio of air (taken to be 1.4)
$Pt_{in,\dot{m}}$	Mass averaged total pressure at the inlet
Pt_{out}	Total pressure at the outlet, measured by the five-hole probe
$Pt_{out,\dot{m}}$	Mass averaged total pressure at the outlet
$Ps_{out,A}$	Area averaged static pressure at the outlet
$C_{P,local}$	Local loss coefficient (mass averaged)
$C_{Pt,\dot{m}}$	Mass averaged overall loss coefficient
$\vec{V}$	Local flow velocity
$\vec{V}_p$	Primary flow velocity
$\vec{V}_s$	Secondary flow velocity
U	Flow velocity magnitude (purge flow calculations)
ρ	Flow density (purge flow calculations)
A	Flow area (purge flow calculations)

Subscripts

x, y, z	Component of velocity in the x, y, z directions, respectively
c	Flow property refers to coolant flow (purge flow calculations)
∞	Flow property refers to main flow (purge flow calculations)

Acronyms

Cx	Axial chord length
CFD	Computational Fluid Dynamics
PS	Pressure Side of the vane
SS	Suction Side of the vane
SKE	Secondary Kinetic Energy
BR	Blowing Ratio
MFR	Mass Flow Ratio

1 Introduction

As gas turbines are used for propulsion and power generation, many people desire to improve efficiencies for the sake of reducing operational costs. Significant work has been done resulting in better understanding of the flow physics as well as knowledge of some methods to improve the efficiency.

A small improvement in the efficiency of either the turbine or compressor of a turbomachine results in a larger change in the overall power output, because the power output is the difference between turbine and compressor work [1]. Losses in turbomachines are historically divided into profile loss, tip leakage loss, and endwall loss. Endwall loss is also called secondary loss, because it partially arises from the secondary flows through the blade passages. The three loss components are similar in magnitude, and each contributes about 1/3 of the total loss. Endwall loss is the most difficult to predict, and most prediction methods depend almost exclusively on empirical data rather than the underlying physics [1]. The endwall flow patterns are determined by the secondary flow, which depends on the upstream boundary layer and the amount of blade row turning. This secondary flow is an inviscid phenomenon, and does not generate any entropy by itself.

Increasing loading allows for fewer blades (reducing weight and cost), but increases the strength of secondary flows [2]. As a result, methods of decreasing these secondary flows are important for maintaining efficiency while increasing loading.

Much research has been done to determine and describe the behavior of secondary flows in turbomachinery. Wang, Olson, Goldstein, and Eckert [3] used smoke wires and a laser light sheet to investigate the secondary flow near the endwall. They presented a model describing the formation of secondary flows that is useful for understanding the qualitative behavior of the secondary flow, and to anticipate sources of potential quantitative improvements. They extended the previous findings of Langston [4, 5], Gregory-Smith [6], and Sieverding [7]. As the flow in the boundary layer approaches the leading edge of the airfoil, a horseshoe vortex system is created, consisting eventually of two vortices (one each on the suction and pressure sides) travelling downstream. The pressure side leg of the horseshoe vortex travels towards the suction side of the adjacent airfoil and merges with the suction side leg of that vortex by forming a counter rotating vortex pair. This vortex pair is dominated by the pressure side leg, and becomes the passage vortex. This motion of the pressure side leg towards the suction side is caused by the cross-passage pressure gradient. The passage vortex entrains the main stream flow and boundary layer, growing in size and moving away from the endwall. Additionally, the passage vortex induces a counter vortex (called a wall vortex by Wang et al.) near the suction surface of the airfoil.

Multiple methods have been attempted in order to reduce the formation of secondary flows. Endwall contouring is one such method, and is the focus of this experiment. The cross-passage pressure gradient creates the secondary flow by sweeping the boundary layer fluid from pressure to suction surface on the endwall [8]. A counterflow at some distance is also generated. The secondary flow increases losses within the blade row. Furthermore, the non-uniform exit flow may cause extra losses in downstream blade rows. The aim of using nonaxisymmetric endwall contouring is to modify the static pressure field on the endwall, changing the secondary flow and hopefully reducing losses. Other methods of attempting to reduce secondary losses include endwall fences [9], endwall jets [10], and leading edge fillets [11].

This study examines the effects of endwall contouring and upstream purge flow on the performance of a nozzle guide vane at transonic conditions. A backward facing step upstream of the leading edge is incorporated in order to better match engine geometry. Loading measurements, downstream five-hole probe traverses, and flow visualization with oils were used to understand the flow behavior.

2 Literature Review

Due to their impact on losses, considerable research has been conducted on understanding, measuring, and reducing secondary flows in gas turbines. In the 1970s and 1980s, the first studies were performed to characterize secondary flow by pressure measurements and flow visualization techniques.

Significant effort has been expended on investigating the use of endwall contouring to reduce secondary losses. Some of this research has been performed on axisymmetric contours, while other research has been done on three dimensional (nonaxisymmetric) contours, as in the current study. A few studies have utilized rotating rigs, while the majority involve linear cascades.

The most relevant rotating rig study was performed by Germain et al [12], who tested 3D endwall contours for a 1.5 stage high work axial turbine with an exit Mach number of about 0.5. They used CFD and optimization codes to design the best endwall profile to use in the experiment. CFD predictions were confirmed with five-hole probe measurements, finding stage efficiency benefits of about 1% and a reduction in SKE of 30%. Improvements in the flow were seen at midspan as well as near the endwall, implying that endwall contouring affects the entire passage. The transition model used on the airfoil has a strong influence on the secondary loss predictions. CFD underestimated the efficiency improvements, so more modeling work is necessary to achieve good predictability.

Many relevant studies have been performed using linear cascades. However, most of these studies have been performed using blades with high turning, rather than nozzle guide vanes. As a result, they are not necessarily directly comparable to the current study, because the amount of turning significantly influences the passage vortex strength.

Hartland et al [8] investigated nonaxisymmetric endwall contours using a low speed linear cascade tunnel at the University of Durham. Downstream five-hole probe traverses and endwall surface static pressure measurements were taken for a nonaxisymmetric contoured endwall as well as a planar endwall. The results were compared to CFD predictions. They measured a reduction in secondary flows and a more unifom flow angle profile, as predicted by CFD. Additionally, they found a reduction in the overall loss, which CFD failed to predict. Some discrepancies between CFD and measurement may be the result of the turbulence model used.

Knezevici et al [13],[14] studied endwall contouring using a low speed wind tunnel at Carleton University. Unlike other studies, they applied contouring to low-pressure turbine airfoils rather than high pressure turbine airfoils. Additionally, they used contouring in conjunction with high-lift airfoils to achieve an optimized design, rather than simply optimizing the endwall for a given airfoil. A seven-hole probe was used to measure the downstream losses. They found a reduction in the cross-passage pressure gradient, leading to a 13% decrease in secondary kinetic energy.

Taremi et al investigated the effects of endwall contouring [15] and blade loading [16] on secondary flows for high turning blades with an exit Mach number of 0.8. They compared four total configurations: flat and contoured endwalls in linear cascades, each with two different blade loadings. They found that the higher loaded configurations exhibited stronger secondary flows. The contoured endwall cases displayed weaker secondary flows than the flat endwall cases, but the difference was much smaller for the low loading cases than high loading. The measurement techniques that were used were similar to the ones used in the current study.

Jain et al [17] investigated the effects of an upstream purge slot and mateface gap on the loss coefficient for a high turning, 3D contoured endwall passage using Virginia Tech's transonic linear cascade tunnel. The exit Mach number was 0.87. They found significant reduction in aerodynamic losses using the contoured endwall in comparison to a non-contoured planar endwall. The addition of coolant flow through the slot did not have a large impact on losses, however there was a small increase in losses near midspan and a decrease between 5% and 25% span. Unlike the rest of the studies in this literature review, this one includes the effects of purge flow and a backward facing step. However, the backward facing step used in this study was much further upstream (relative to its height) than the current study.

The one study using 3D contoured endwalls with nozzle guide vanes was performed by Brennan [18], using Virginia Tech's transonic cascade tunnel. This study used the same airfoil profile as the current study, however, it did not include a backward facing step or upstream purge flow. Brennan found a small improvement in aerodynamic performance.

While there has been extensive research on endwall contouring, the majority of this research has been performed at subsonic conditions, and is therefore not directly comparable to the current study, which is performed at transonic conditions. Additionally, most of the existing literature focuses on high turning airfoils used as rotor blades, while the current study investigates low turning airfoils used as stator vanes. This is an important distinction because the passage vortex strength is directly impacted by the amount of turning (more turning leads to a stronger passage vortex). The current study also includes a backward-facing step upstream of the vane row leading edge, and purge flow injected on this step, resulting in a different geometric configuration than the existing literature. None of the existing literature investigates a 3D contoured endwall, applied to a passage of nozzle guide vanes, with the effects of upstream purge flow and a backward facing step.

3 Experimental Setup

3.1 Virginia Tech Transonic Wind Tunnel

All experiments were conducted in the transonic cascade wind tunnel at Virginia Tech. This is a blowdown facility, and can operate for 30 seconds at Mach numbers up to and in excess of 1. The test sections are interchangeable in order to perform a variety of experiments on turbomachinery components. Figure 2 shows a schematic of the wind tunnel.

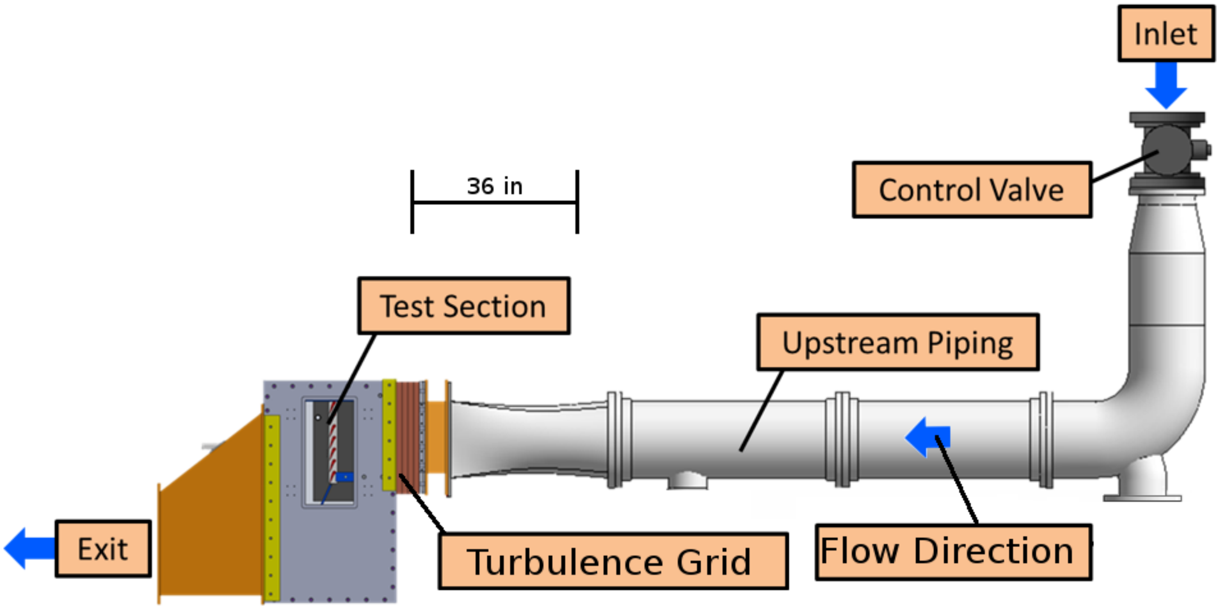

Figure 1. Virginia Tech's Transonic Wind Tunnel

Prior to a run, two storage tanks are pressurized to 150 psi by a four-stage Ingersoll-Rand compressor. The safety valve and butterfly valve open at the beginning of a run, which allows air to pass through an upstream settling chamber, the flow contraction, and the turbulence grid before entering the test section. The butterfly valve acts as a control valve, and is controlled by a LabVIEW program in order to maintain a steady inlet pressure. The program progressively opens the valve according to a predefined sequence in order to counteract the dropping pressure in the storage tanks.

3.2 Test Section Details

A similar test section was used by Brennan to test inlet guide vanes with the same profile as the current project, but without the backward facing step and upstream purge flow; more details can be found in [18]. Another test section was used by Peterson to test high pressure, high turning turbine blades; details can be found in [19].

Flow passes through a contraction and a turbulence grid before entering the linear cascade. The turbulence grid was placed 8.8 Cax upstream of the leading edge and induced a free-stream turbulence intensity of 3.5% with a length scale of 0.827 inches. The flow passes through the vanes and then exits out the back of the test section to atmospheric conditions. The linear cascade is made up of six inlet guide vanes and five passages, with a movable headboard and lower tailboard to improve periodicity in the flow. Figure 2 depicts a schematic of the linear cascade can be seen.

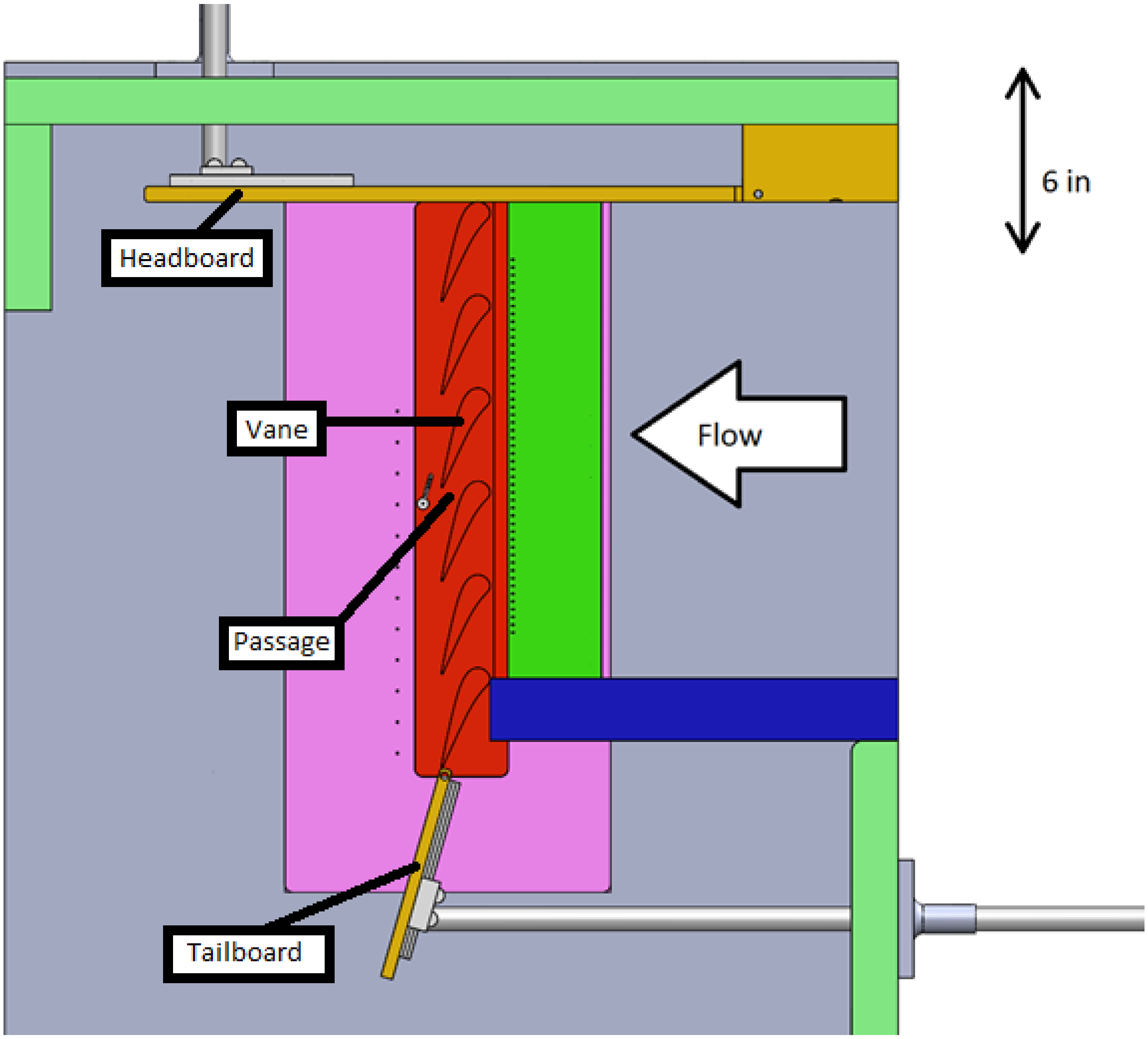

Figure 2. Side view of linear cascade with the window removed and no side wall

The five-hole probe was inserted through test slots downstream of the vanes in order to take aerodynamic measurements. The central passage and the two half-passages on either side were chosen as the passages of interest and all measurements were taken on the flow passing through them. The slots were long enough to cover two entire passages of flow. Figure 3 shows the passages where measurements were taken. Yellow lines have been added to show the outlet flow angles for the central vanes. The lighter blue region indicates the passages of interest.

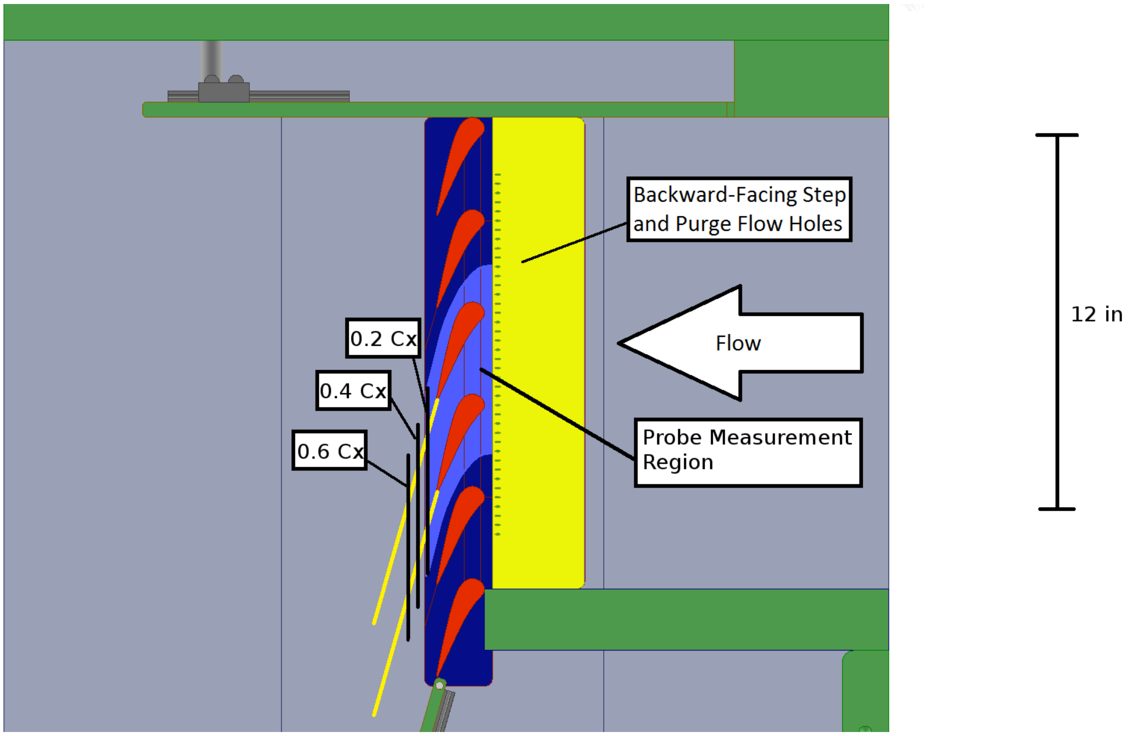

Figure 3. Side view of the test section. Measured passages can be seen through the transparent window.

The upstream purge flow was injected through two staggered rows of holes on the backward-facing step. A schematic for this is shown in Figure 5. More details are available in Appendix C.

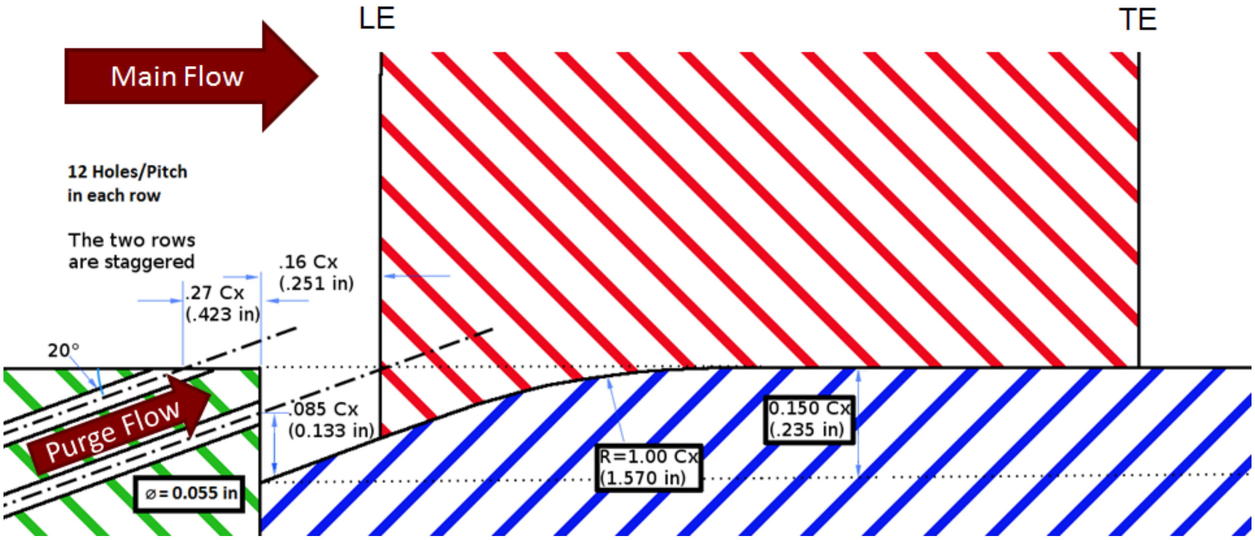

Figure 4. Upstream geometry schematic.

3.3 Vane and Endwall Details

Inlet guide vanes designed by Honeywell Aerospace were used in the test section. Six vanes were used to create five passages for the flow, with the top and bottom vanes mating to the test section boundaries. All vanes were 3D printed, using a Fortus 250mc printer. A picture of the linear cascade can be seen in Figure 5. Additional information regarding the vanes can be found in Appendix B.

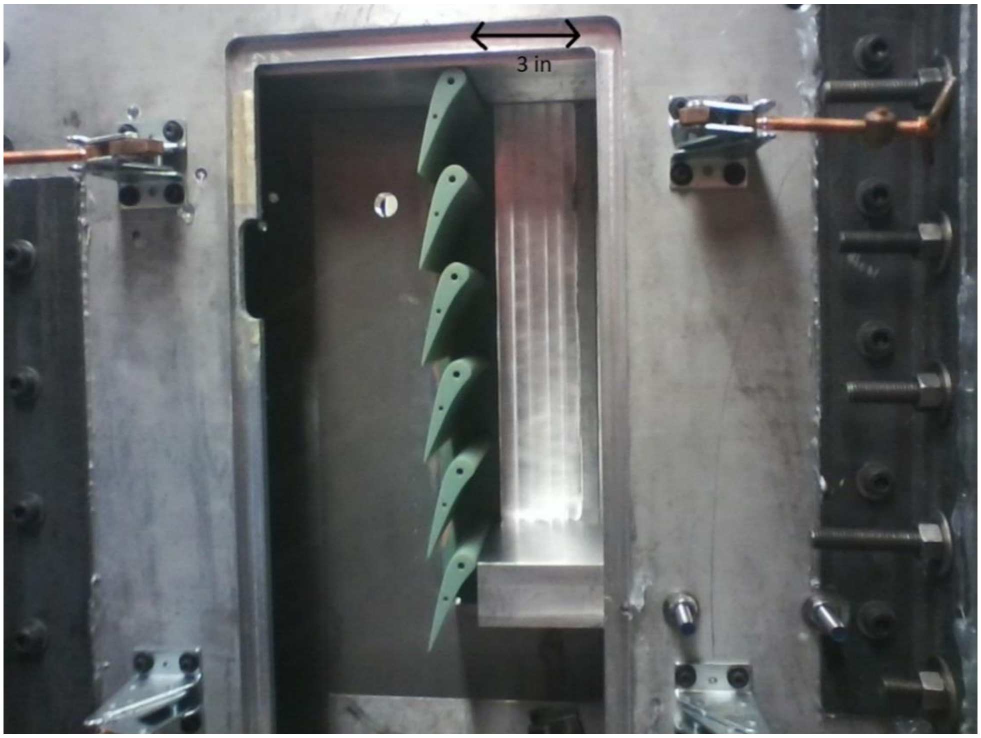

Figure 5. Linear cascade with window removed. Lower tailboard is not present in the picture.

Interchangeable endwalls were used so that the contoured and flat endwalls could be tested on the same window. Figure 6 shows the endwalls used in the experiment. The flat endwall was printed in three pieces, with the top and bottom pieces having two integrated vanes each. The middle piece instead has cutouts for separate vanes to be attached. The contoured endwall was 3D printed as a single piece, with six cutouts for vanes to be attached

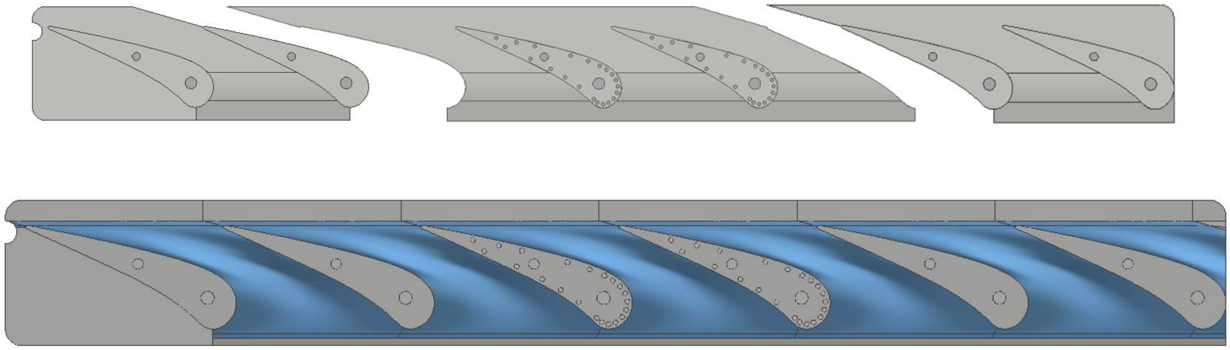

Figure 6. Tests were performed with a flat endwall (Top) and contoured endwall (Bottom)

3.4 Upstream Purge Flow

Purge flow may be characterized by several parameters comparing the main flow to the injected flow. These parameters are typically expressed as a ratio of the cooling flow to the main flow. These include the velocity ratio and density ratio:

$$Density\ Ratio = \frac{\rho_c}{\rho_\infty}$$

$$Velocity\ Ratio = \frac{U_c}{U_\infty}$$

In order to accurately replicate the conditions in the engine, the blowing ratio is matched. This is defined as the product of the density and velocity ratios:

$$BR = Blowing\ Ratio = (Density\ Ratio) * (Velocity\ Ratio) = \frac{\rho_c U_c}{\rho_\infty U_\infty}$$

Additionally, the mass flow ratio is defined. For a given geometry, the mass flow ratio is proportional to the blowing ratio, so if the mass flow ratio is matched the blowing ratio is matched as well.

$$MFR = Mass\ Flow\ Ratio = \frac{\dot{m}_c}{\dot{m}_\infty} = \frac{A_c \rho_c U_c}{A_\infty \rho_\infty U_\infty} = \frac{A_c}{A_\infty} * BR$$

The mass flow of the coolant flow is determined directly using a mass flow meter, while the main flow mass flow is estimated by measuring the density and velocity at midspan:

$$MFR = \frac{\dot{m}_c}{A_\infty \rho_\infty U_\infty}$$

Due to the geometric relationship between blowing ratio and mass flow ratio:

$$BR = \frac{\dot{m}_c}{A_\infty \rho_\infty U_\infty} \frac{A_\infty}{A_c} = \frac{\dot{m}_c / A_\infty}{\rho_\infty U_\infty}$$

A_∞ was calculated using only the four passages (three complete and two half passages) that had cooling flow applied. This was considered a better comparison to the engine geometry than to use the full five passages of main flow, because the regions without cooling will have little effect on the passages of interest (the middle passage and two neighboring half passages).

Main flow density and velocity were determined using upstream total pressure and static pressure probes as well as an upstream thermocouple.

3.5 Test Configurations

Three test configurations were used in the experiment and are summarized in Table 1. The current study is examining the effects of endwall contouring and of upstream purge flow. All cases have the backward facing step upstream of the vane row. Results from each test will be discussed in the following section. Blowing is quantified as the blowing ratio (BR).

Table 1. Test configurations for the experiment

Test	Blowing	Endwall
1	No	Flat
2	Yes, BR = 1.5	Flat
3	Yes, BR = 1.5	Contoured

4 Results and Discussion

Results from vane loading will be presented first, then surface oil flow visualizations, and downstream probe measurements. Downstream survey data was checked for repeatability; details on repeatability are in Section F of the appendix. An uncertainty analysis was also performed on downstream survey data, which is in Section G of the appendix.

4.1 Vane Loading

Vane loading data was taken on the two vanes surrounding the central passage. The vanes were instrumented with static pressure taps, which are described in more detail in Section 0. Figure 7 shows which vane surfaces that were instrumented as well as the terminology used to denote each surface. Loading measurements were taken at 4% span.

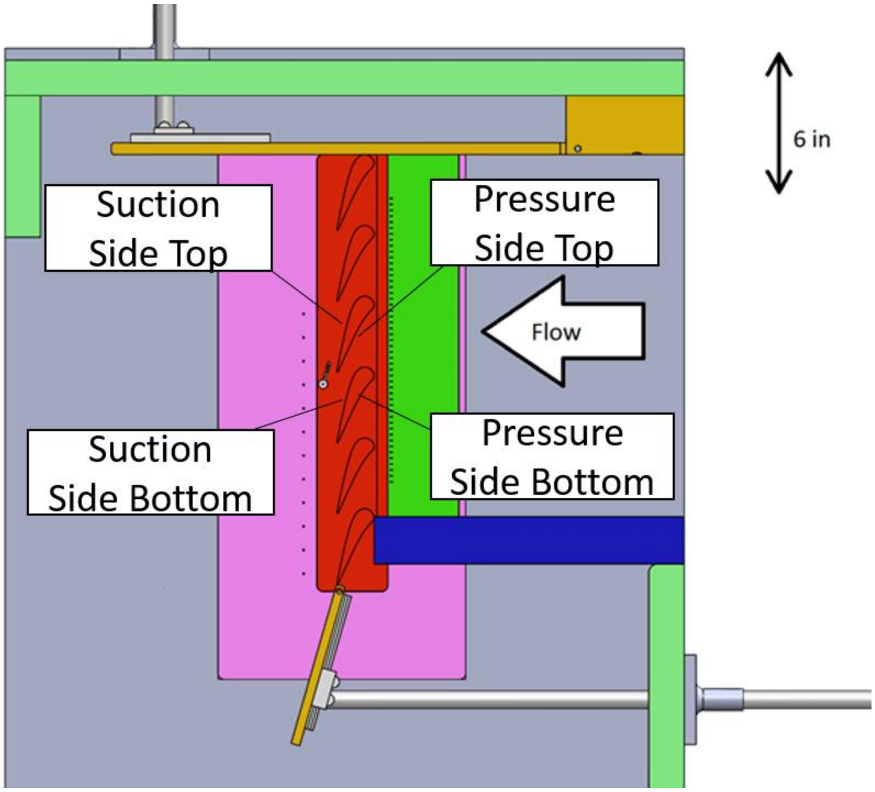

Figure 7. Location of loading measurement locations

Vane loading was displayed using isentropic Mach number as a function of axial chord. The local isentropic Mach number along the surface of the blade was calculated using Equation (1)

$$M_{isen} = \sqrt{\frac{2}{\gamma - 1}\left(\frac{Ps_{surf}}{Pt_{in}}^{\frac{1-\gamma}{\gamma}} - 1\right)} \tag{1}$$

Figure 9 shows the results from 50% span measurements. This measurement was taken to compare with CFD and to verify periodicity. The flow on the suction side steadily accelerates up to about 60% chord, goes through a shock, and then decelerates slightly before the trailing edge. The experiment and CFD agree well, and periodicity is good. There is some aperiodicity near the leading edge, which is likely due to the rapid change in Mach number vs. axial position at this point. The overall good periodicity and match with CFD helped establish that the vane profile and wind tunnel conditions were met correctly.

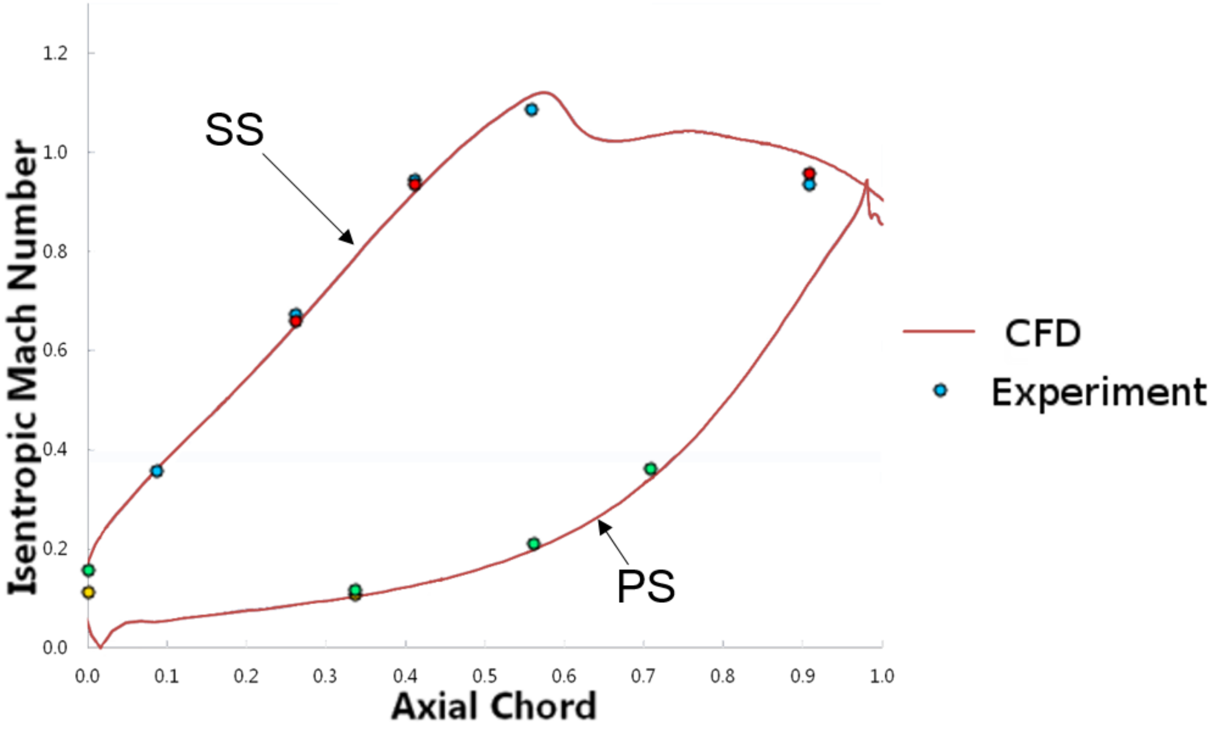

Figure 8 Loading data, 50% span, Flat Endwall without Blowing

Loading measurements were also taken at 4% span for all three configurations in order to determine the effect of the endwall. These are shown in Figures 10 through 12. Once again, periodicity is good overall between the two vanes. The location with the worst periodicity is in the proximity of the shock. This is consistent with previous experiments [19]. The flow near the shock is difficult to predict and is very sensitive to slight disturbances, so this is physically reasonable.

Figure 13 shows a comparison between the loading for the contoured and flat endwalls. No significant differences are observed.

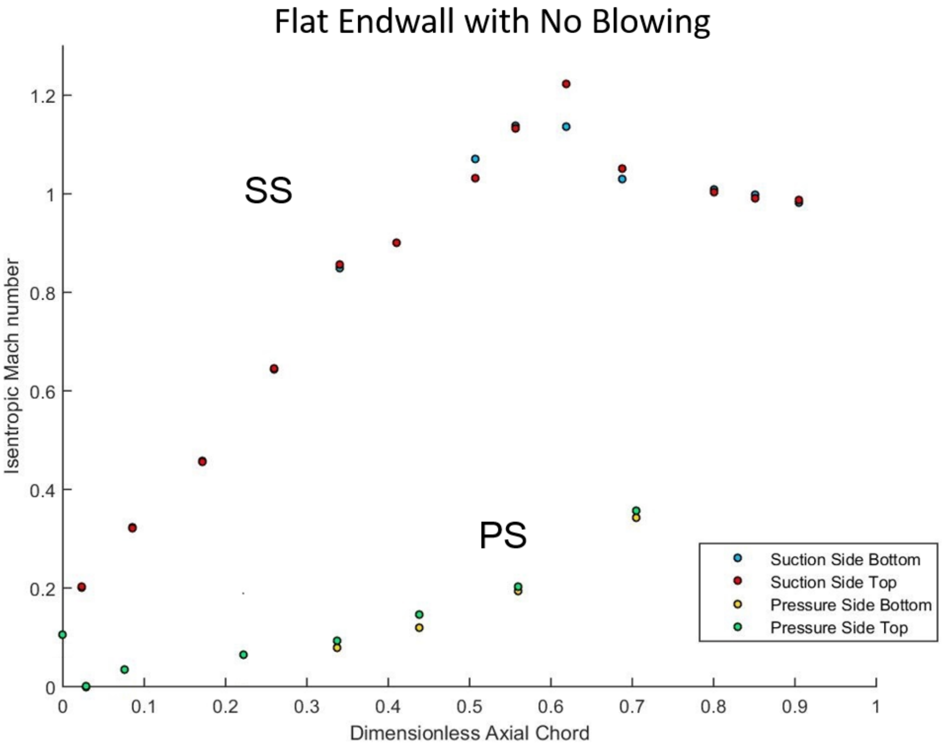

Figure 9. Loading for the flat endwall case without blowing at 4% span

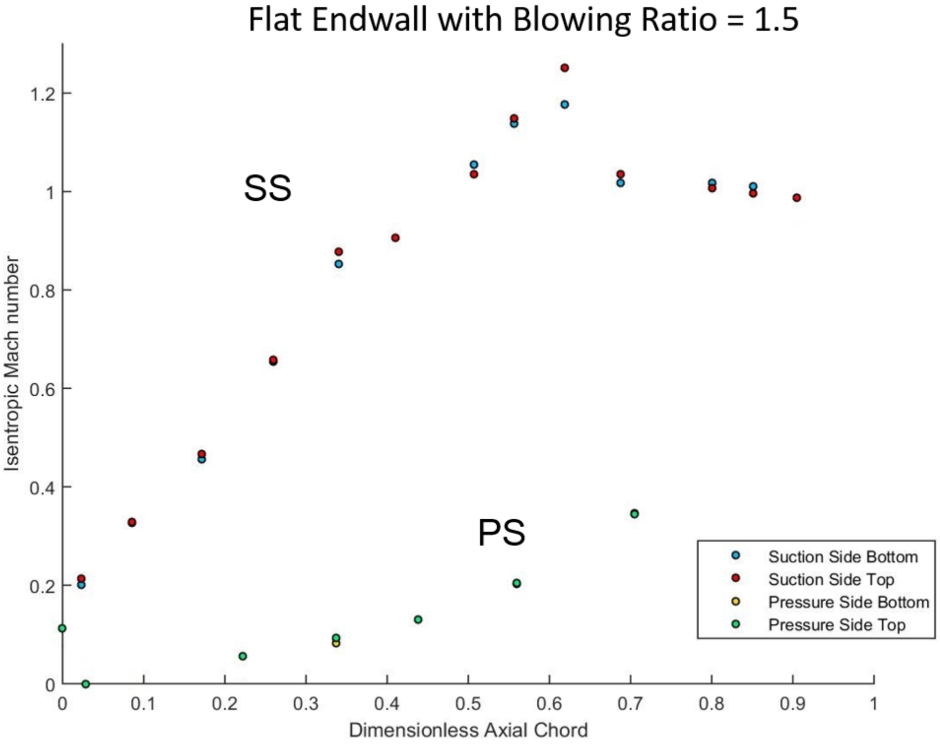

Figure 10. Loading for the flat endwall case with a blowing ratio of 1.5 at 4% span

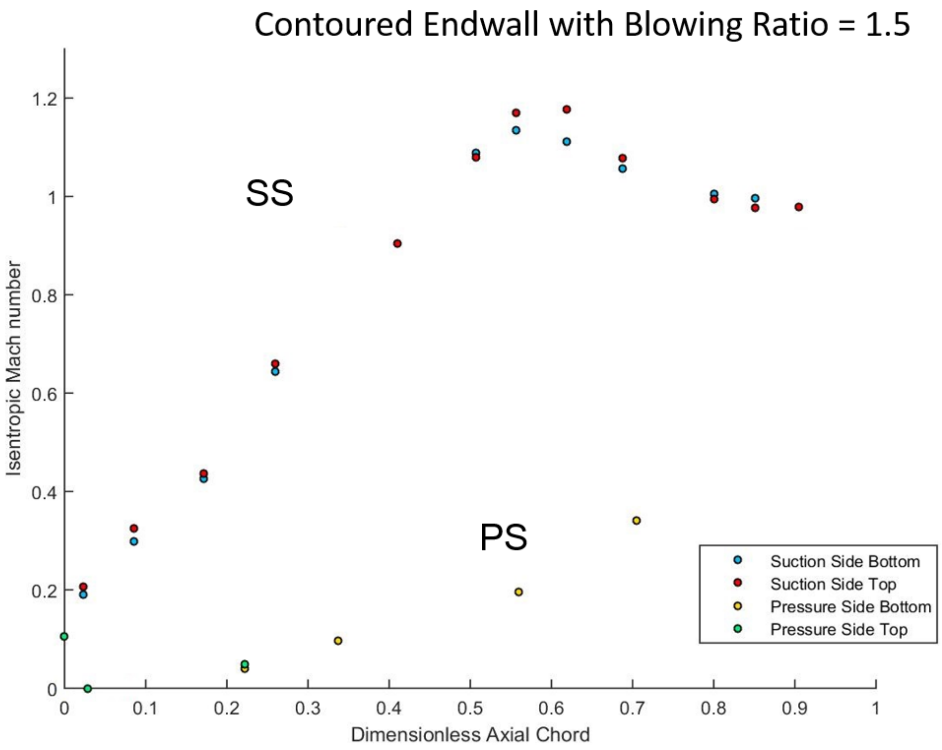

Figure 11. Blade loading data for contoured endwall test configuration at 4% span

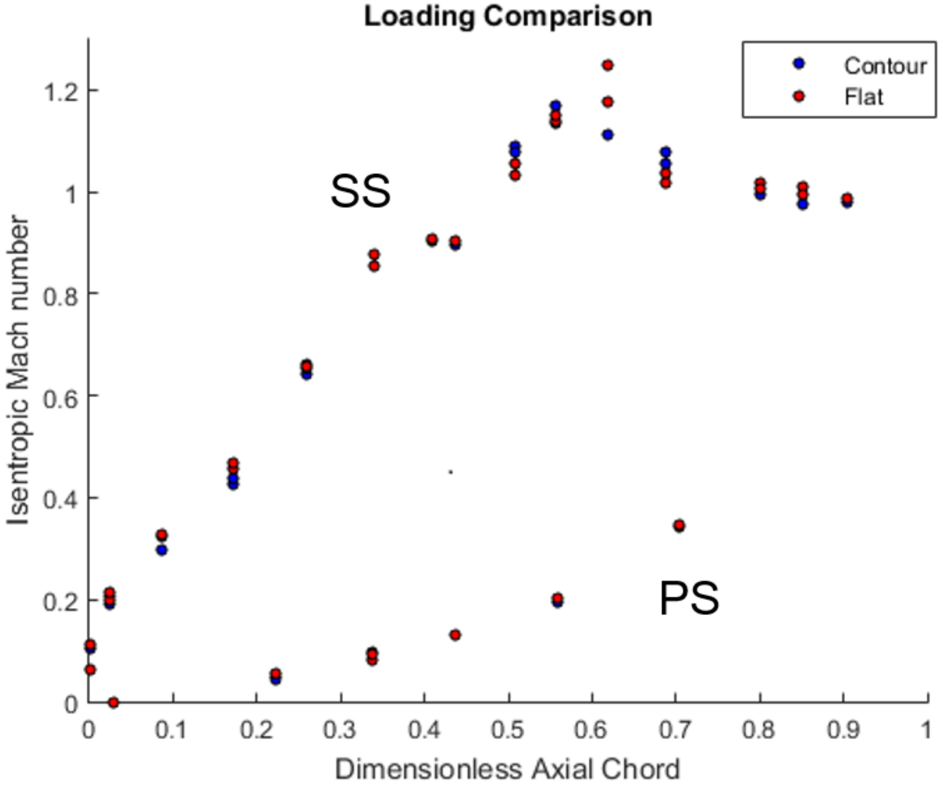

Figure 12 Loading comparison between flat and contoured endwalls with a blowing ratio of 1.5

4.2 Flow Visualizations

Flow visualizations were conducted using colored oils, in order to qualitatively understand the flow physics. Oils were painted onto the surfaces of the endwall and the backward-facing step and used to track the flow downstream. Figure 13 shows a picture of the test section before the blowdown. A line of yellow oil was placed approximately just downstream of the backward-facing step, pink oil was applied to the pressure sides of the vanes, and blue oil was applied to the suction side near the leading edge. A line of green oil was applied to the edge of the backward facing step in hopes of visualizing reattachment; this was unsuccessful and was not used in later tests.

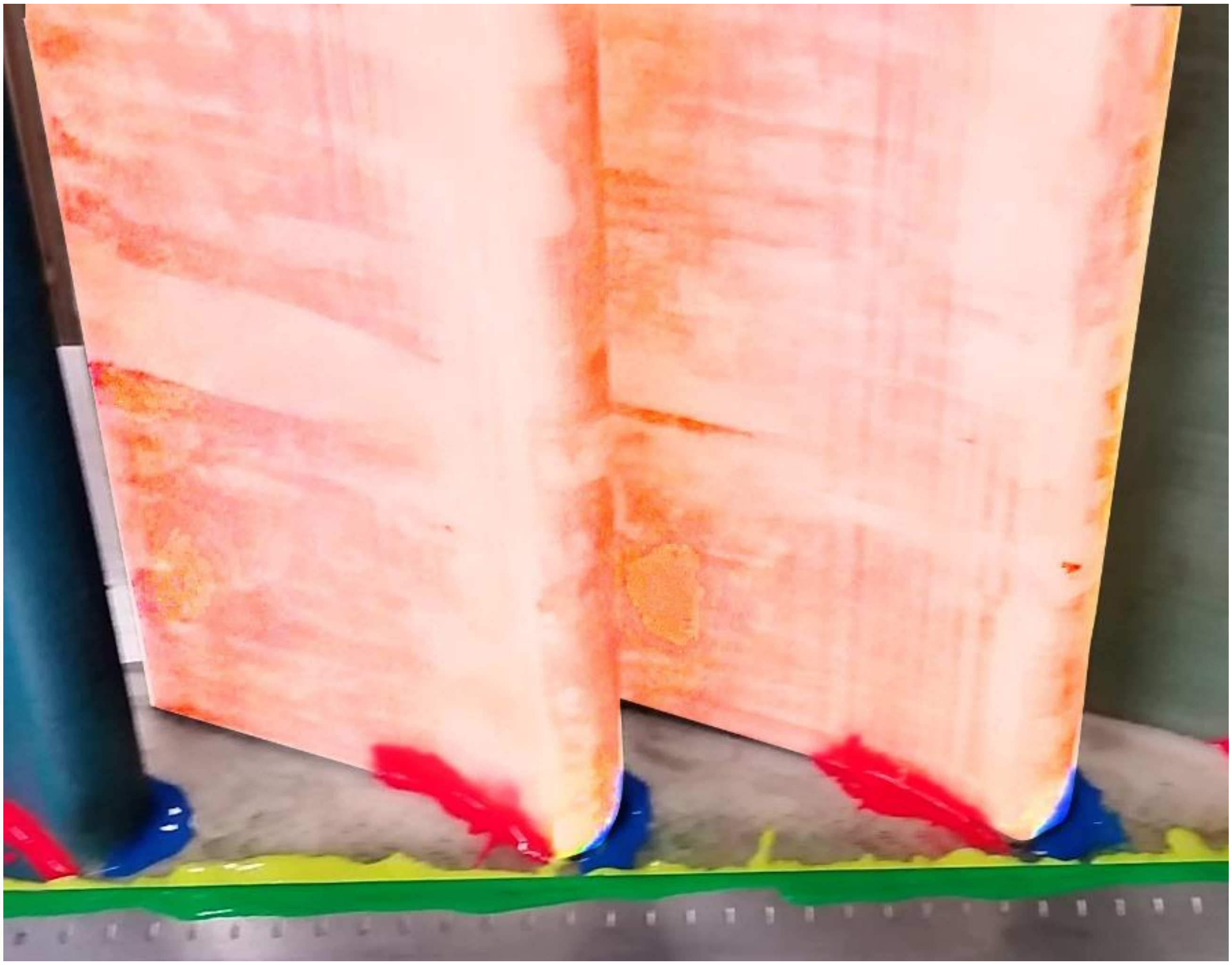

Figure 13. Before (Left) and after (Right) pictures for flow visualization tests

Following the blowdown, the windows were removed and the flow patterns in the oil were observed. Measurements were taken of five different flow features after the run, and these locations are depicted in Figures 15 and 16. Pictures were taken after blowdown. All pictures for flow visualization have been digitally edited in order to improve the visibility of the oil on the vanes and endwall.

Figure 15 shows the pressure side of one of the vanes after a blowdown. The blue oil on the suction side of the vane is pulled slightly forward of the leading edge by the suction side leg of the horseshoe vortex. This is visible on the right edge of the picture (measurement A). This measurement was similar between the two flat endwall cases, and was increased by 37% by the contoured endwall. The height of the red oil applied to the pressure side is also measured (B). This is the parameter that varied the most (only 0.4 inches for the flat endwall no blowing case, compared to 1.87 and 3.3 inches for the flat and contoured with blowing cases, respectively). However, it is uncertain whether the difference in this feature was the effect of real changes in the steady-state flow field, or if the increased height was simply caused by the influence of the purge flow prior to running the tunnel. Due to the experimental setup, the purge flow was started anywhere from a minute to three minutes before blowdown, and this may have displaced the pressure side paint prematurely.

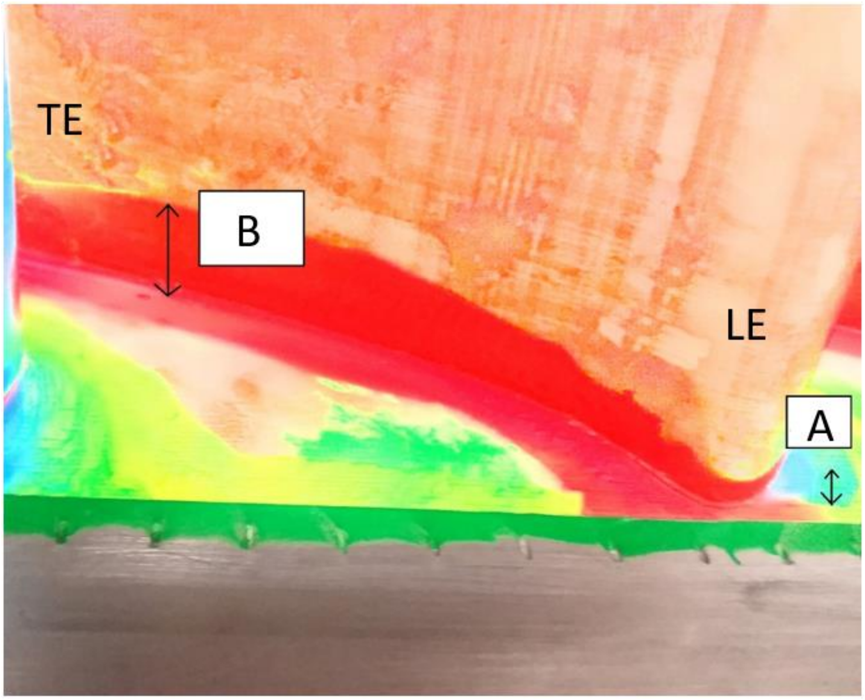

Figure 14. Features measured in flow visualization (view of pressure side)

Figure 16 shows the suction side of a vane after blowdown. Measurement C is the length of the region of contact of the inlet boundary layer with the suction side of the vane (yellow oil). This region is very similar in length for the two flat endwall cases, and is about 33% shorter for the contoured endwall case. This is consistent with the results of Brennan [18], and suggests that the contoured endwall entrains less boundary layer flow in the passage vortex.

The most important measurements concern the passage vortex. Measurement D is the distance between the trailing edge and the lift off point of the passage vortex, and measurement E is the spanwise location of the passage vortex at the trailing edge. The passage vortex lifts off earlier but stays closer to the endwall for the flat endwall no blowing case as compared to flat endwall with blowing. This is consistent with the observations from five-hole probe measurements (Section 4.3). The contoured endwall exhibits an earlier liftoff of the passage vortex, as well as greater penetration spanwise into the passage, than the flat endwall (both cases with blowing). This is consistent with the five-hole probe results, as well as the earlier results by Brennan.

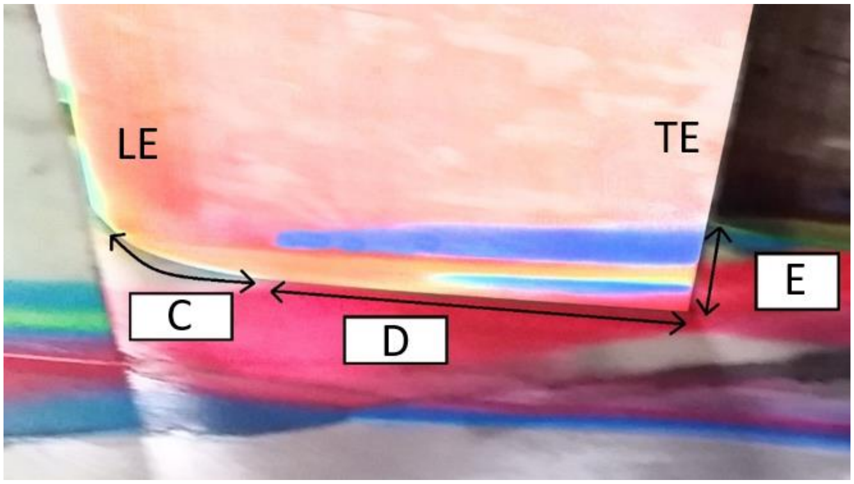

Figure 15. Features measured in flow visualization (view of suction side)

Table 2. Qualitative comparison of flow visualizations from flat and contoured endwalls

Comparison of Flow Visualization Measurements					
(dimensions in inches, ±0.05 in accuracy)	A	B	C	D	E
Flat, No Blowing	0.16	0.4	0.74	2.27	0.79
Flat, BR=1.5	0.16	1.87	0.76	2.46	0.68
Contoured, BR=1.5	0.22	3.3	0.5	2.67	0.78

4.3 Downstream Measurements

All downstream measurements were taken with a five-hole probe manufactured by Aeroprobe. The specifications for this probe can be found in Section 0. An airtight traverse box was mounted outside of the test section and contained the equipment to hold and move the five-hole probe. Additional description of the traverse box setup can be found in Section 8.4. Measurements were taken 0.2 Cx, 0.4 Cx, and 0.6 Cx downstream of the blade row. A slot nearly 2 full pitches in length was machined into the window at each of these locations to allow the probe head to traverse the exit flow.

After the flow reached steady state, the probe was traversed at 1"/sec in the pitchwise direction while sampling at 10 Hz. The probe was held in the same spanwise position for a particular blowdown and then re-positioned between runs. 11 spanwise locations, spaced logarithmically, were measured in order to create a sample grid of 61x11 data points. A schematic showing the spanwise locations measured by the probe is included as Figure 16.

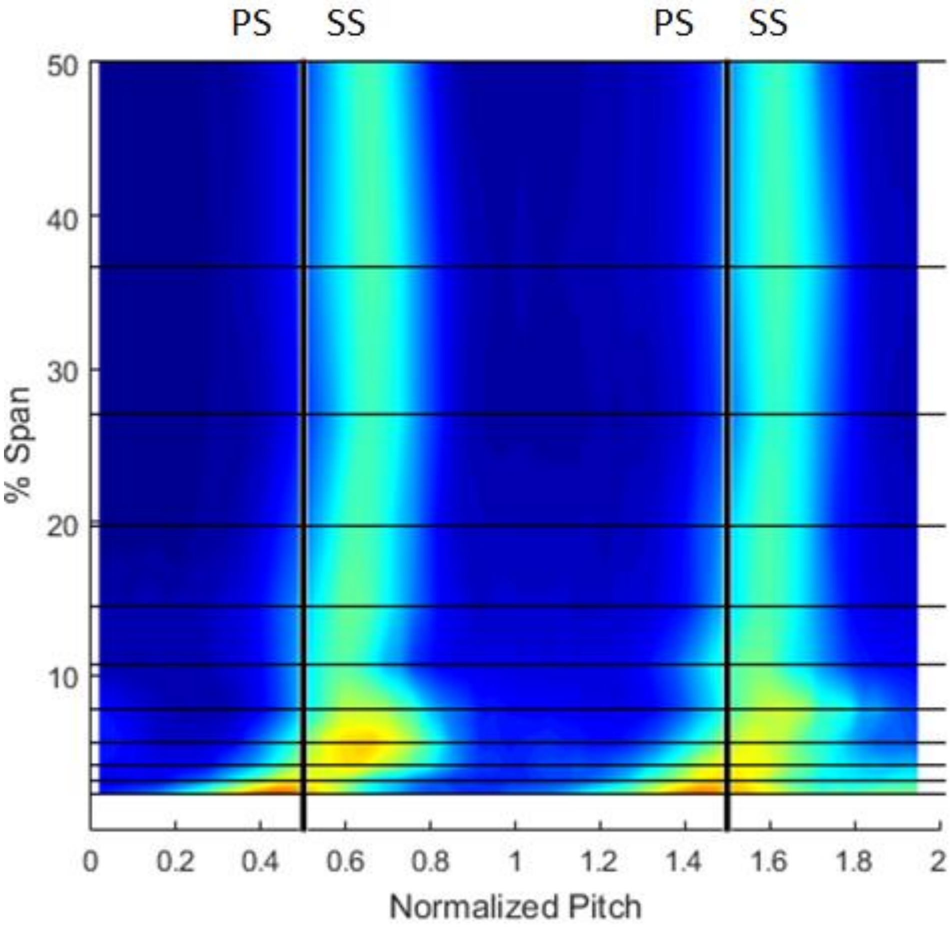

Figure 16. Probe measurement locations

At each location, the five-hole data was used to calculate the local loss coefficient, overall loss coefficient, secondary velocity, secondary kinetic energy, and swirl angle. Values for secondary velocity and secondary kinetic energy were calculated using the methodology from Honeywell's internal documents [20].

4.3.1 Local Loss Coefficient

The local loss coefficient was calculated at every location using equation (2) to quantify the losses through the vane row. The inlet total pressure and outlet total pressure in the calculation are for each individual point. The outlet total pressure is averaged across the entire exit plane, weighted by the mass flow at each point (a mass average). The exit static pressure uses an average across the exit plane weighted by the area at each point. All inlet total pressures were measured at midspan.

$$C_{P,local} = \frac{Pt_{in} - Pt_{out}}{Pt_{out,\dot{m}} - Ps_{out,A}} \tag{2}$$

A local loss coefficient was determined at each point in the grid and a series of contour plots were created. Figures 18 and 19 show the results for each configuration (flat endwall without blowing, flat endwall with a blowing ratio of 1.5, and contoured endwall with a blowing ratio of 1.5) and exit plane (0.2 Cx, 0.4 Cx, and 0.6 Cx downstream of the trailing edge). Profile losses can be seen at all spanwise positions. The peak in loss found between 5% and 10% span can be attributed to the passage vortex and counter vortex. The contoured endwall spread losses further into the passage than the flat endwall at each location (Figure 19).

Because data was not reported in the region between the endwall and 2.3% span, the corner vortex is not visible at 0.2 Cx for the flat endwall, and is only just barely visible at 0.4 Cx and 0.6 Cx as it grows in size (see Figure 19). However, the corner vortex is visible for the contoured endwall at all locations, as it appears to penetrate further into the passage, which is consistent with the flow visualization results. Taremi and Sjolander [15] found that the corner vortex location is altered by changes in the cross-passage pressure gradient, and therefore the corner vortex can be shifted by endwall contouring.

A mass average of this same data was performed at each spanwise position, and is shown in Figures 20 and 21. These figures show peaks in losses at around 5% span for axial positions of 0.2 Cx and 0.6 Cx DS, corresponding to the passage vortex. There is no peak at 0.6 Cx, but there are still noticeable bulges around 5-15% span. This is likely because the passage vortex has spread out sufficiently at this distance downstream that it no longer leads to a sharp peak in losses, but instead an increase over a wider area. The plots also show the effects of the corner vortex near the wall, which rise as the flow proceeds downstream. This is expected as the corner vortex continues to grow as it travels downstream.

These two dimensional profiles of the loss coefficients match shapes well with the existing literature, such as the results of Knezevici and Sjolander [13]. The contoured endwall redistributes losses, resulting in lower loss at the peak due to the passage vortex, but slightly higher losses at midspan as well as very close to the wall. Additionally, the passage vortex is spread over a larger spanwise area, so it still contributes comparable losses overall even though the peak losses are lower. Overall, there is no statistically significant difference in the loss coefficient (this will be discussed in more detail in the next section) but the losses are distributed more evenly in the contoured endwall case.

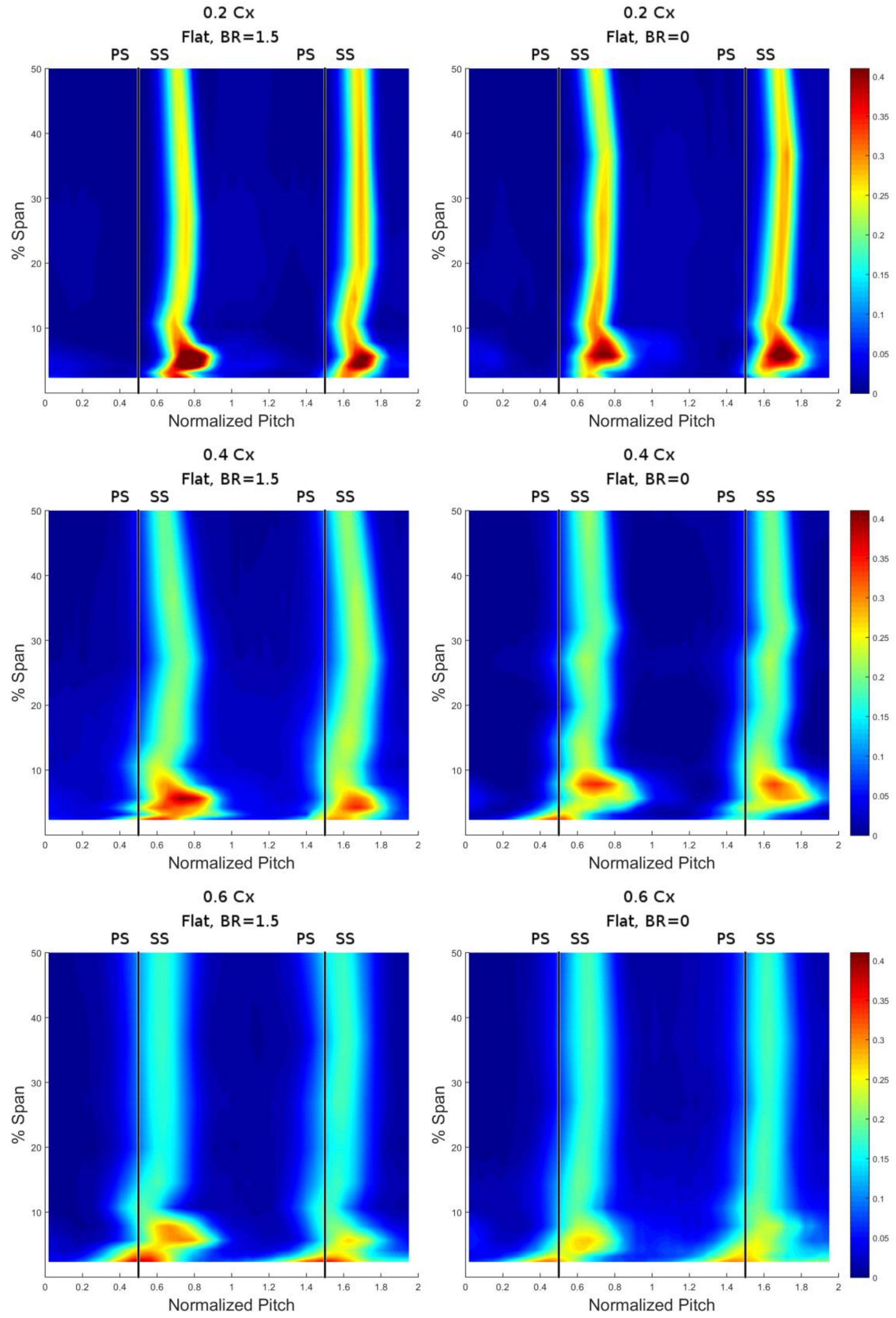

Figure 17. Local loss coefficient for flat endwall with blowing (Left) and flat endwall without blowing (Right) at 0.2 Cx (Top), 0.4 Cx (Middle), and 0.6 Cx (Bottom)

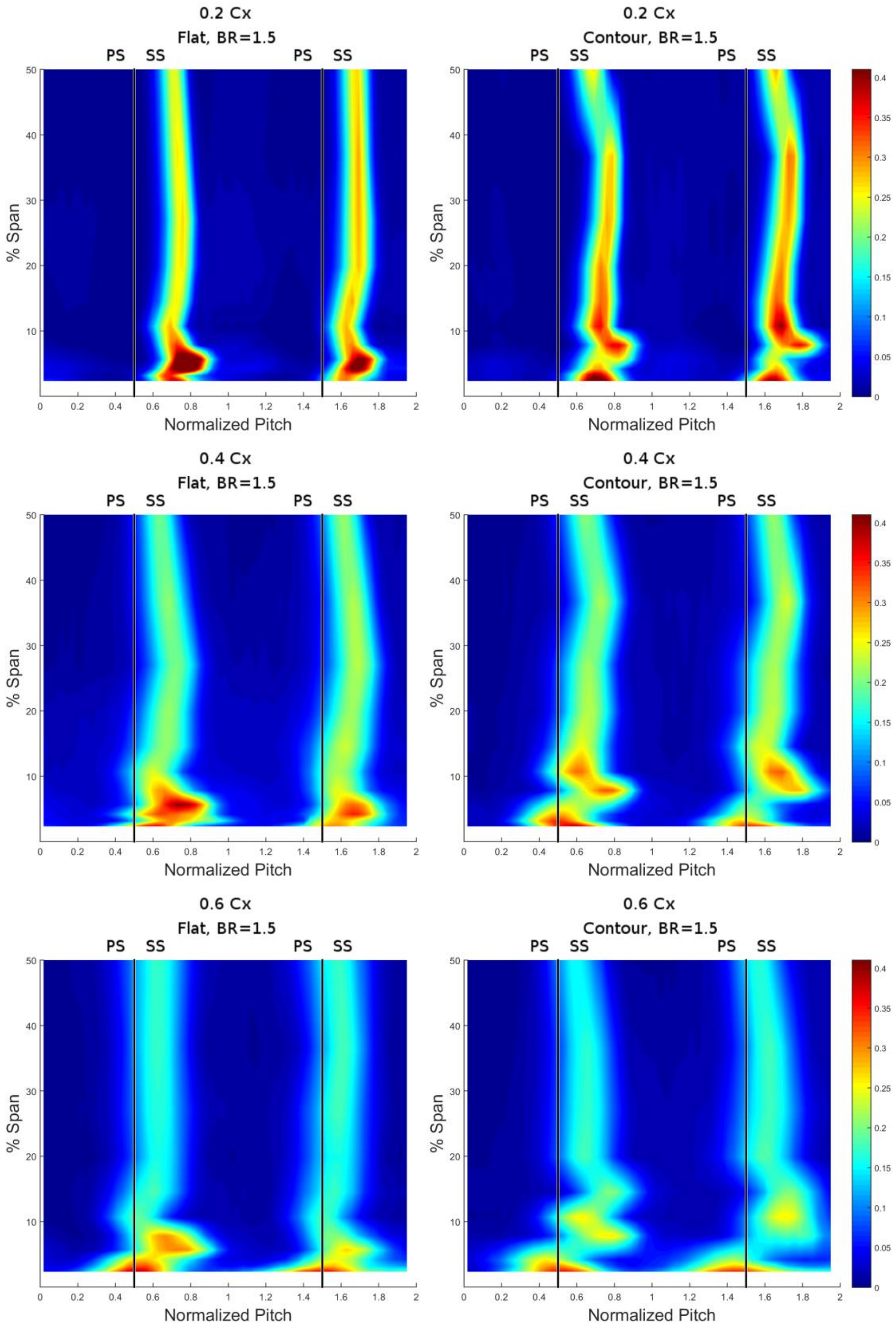

Figure 18. Local loss coefficient for flat endwall with blowing (Left) and contoured endwall with blowing (Right) at 0.2 Cx (Top), 0.4 Cx (Middle), and 0.6 Cx (Bottom)

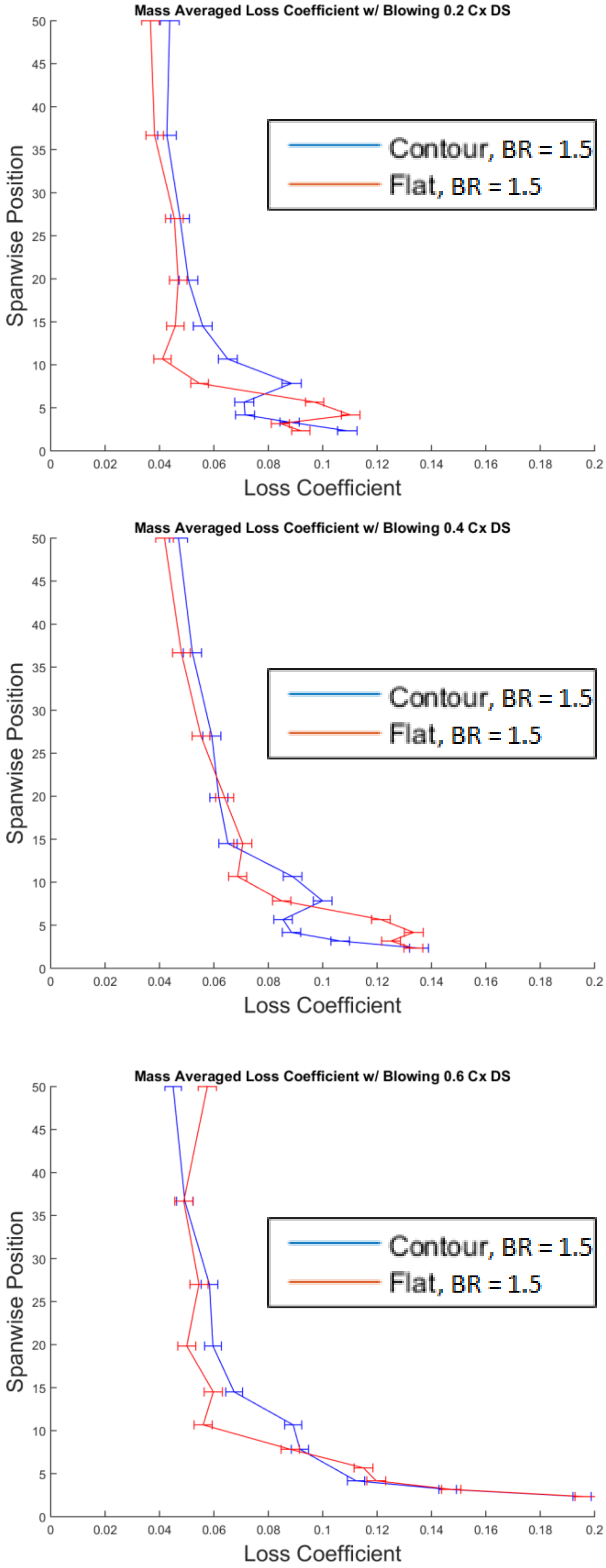

Figure 19. Comparison between flat and contoured endwall cases for mass averaged loss coefficient for each spanwise position

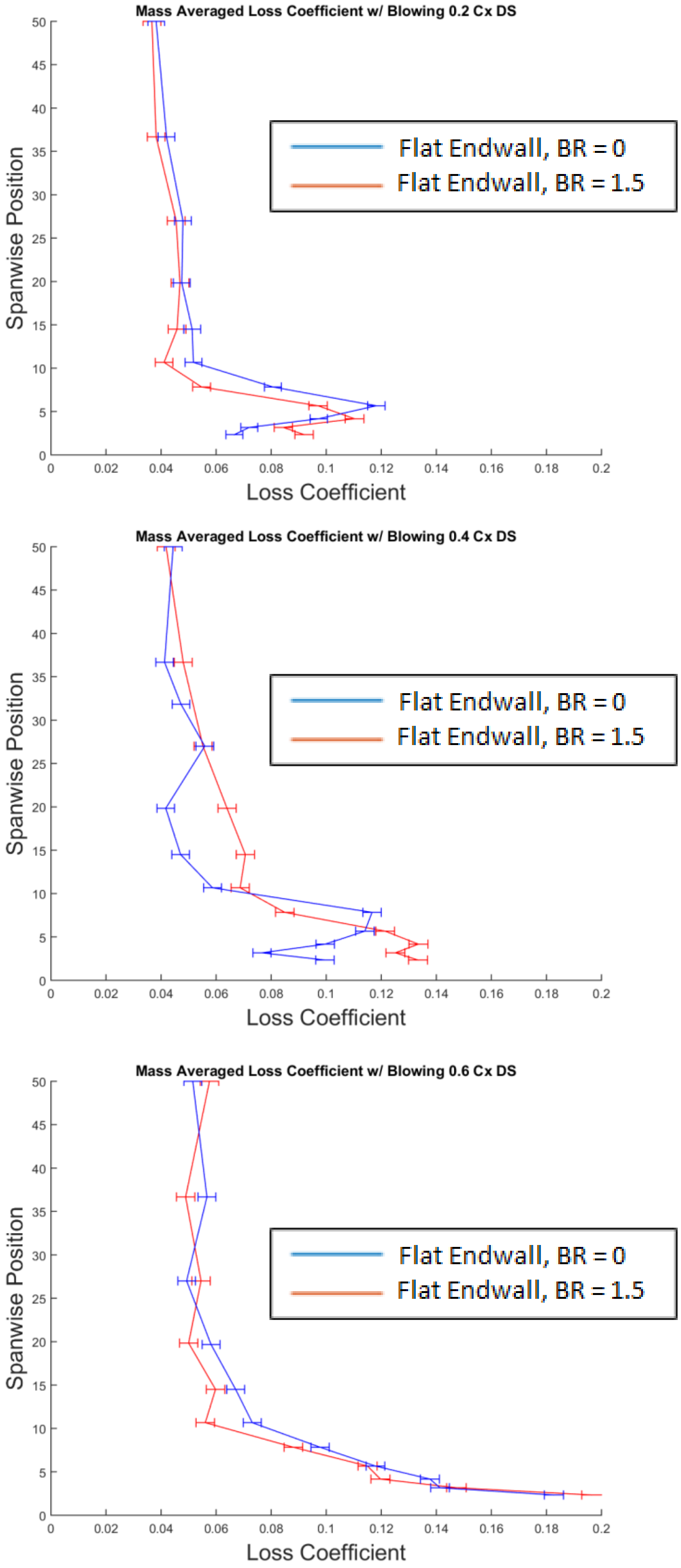

Figure 20. Comparison between blowing and no blowing for mass averaged loss coefficient for each spanwise position

4.3.2 Overall Loss Coefficient

A mass averaged loss coefficient was calculated for every test case in order to compare the overall results. This was calculated by taking a weighted average of the local loss coefficient at each location. This is shown in Equation (3):

$$C_{P_t,\dot{m}} = \frac{\sum \dot{m}_i C_{p,i}}{\sum \dot{m}_i} \tag{3}$$

This average is performed over every data point taken by the five-hole probe, pitchwise and spanwise. The results are summarized in Table 3 for comparing contoured and flat endwalls and Table 4 for comparing blowing and no blowing with a flat endwall. Overall error bounds are determined by taking the upper and lower bounds for each individual local loss coefficient when performing the summation in Equation (3).

Table 3. Mass averaged loss coefficient for each case

Mass Averaged Loss Coefficient (Contoured vs. Flat Endwall, BR=1.5)						
Flat, No Blowing	0.0503	±0.00305	0.0542	±0.00325	0.0654	±0.00325
Flat, BR=1.5	0.0465	±0.00325	0.0607	±0.0033	0.0620	±0.00335
Contoured, BR=1.5	0.0524	±0.00345	0.0623	±0.00335	0.0629	±0.00305

None of the observed differences are larger than the error margins, due to the large relative uncertainty in the loss coefficient.

4.3.3 Secondary Velocity

Secondary velocity measures the magnitude of the local flow travelling perpendicular to the primary flow of the cascade. Essentially, it is a measure of the component of the flow that is not travelling in the main flow direction. High secondary velocity magnitudes mean there is significant flow going in unintended directions, while low secondary flow velocity means that most of the flow is going in the intended direction. This is of interest because the turbine is designed to efficiently utilize flow in the primary flow direction, but flow in any other direction will lead to losses and a resulting drop in efficiency.

At any given point, the velocity vector can be broken down into its components in each Cartesian direction, as shown in equation (4):

$$\vec{V} = V_x\hat{\imath} + V_y\hat{\jmath} + V_z\hat{k} \tag{4}$$

There are multiple reasonable ways to define the primary velocity of the flow. The local velocity at a single location could be used, or multiple local velocities (potentially the entire measured region) could be averaged. Either an area-weighted or mass-flow-weighted average could be used. For this experiment, the primary flow was taken to be the average of all pitchwise locations at midspan, performed using a mass-weighted average. Midspan was chosen because it should not be influenced by the endwall effects. The calculation of primary velocity is shown in Equation (5).

$$\begin{gathered}\vec{V_p} = V_{p,x}\hat{\imath} + V_{p,y}\hat{\jmath} + V_{p,z}\hat{k} \\ V_{p,x} = \frac{1}{\sum \dot{m}_i}\sum \dot{m}_i V_{i,x} \\ V_{p,y} = \frac{1}{\sum \dot{m}_i}\sum \dot{m}_i V_{i,y} \\ V_{p,z} = \frac{1}{\sum \dot{m}_i}\sum \dot{m}_i V_{i,z}\end{gathered} \tag{5}$$

Finally, the secondary velocity is calculated as the difference between the local secondary velocity and the projection of the local velocity vector in the primary velocity direction. This is shown in Equation (6).

$$\overrightarrow{V_s} = \vec{V} - \left(\frac{\vec{V} \cdot \overrightarrow{V_p}}{\left|\overrightarrow{V_p}\right|^2}\right)\overrightarrow{V_p} \tag{6}$$

Figures 22 and 23 report the secondary velocity magnitudes (SVM) for the three cases (contoured vs. flat in Figure 22, flat with vs. without blowing in Figure 23). The higher values of SVM (due to the passage and counter vortices) penetrate further into the passage for the contoured endwall compared to the flat endwall (with a blowing ratio of 1.5 for both cases). Additionally, this region of increased SVM is larger for the contoured endwall case. Peak values of secondary velocity magnitude are spread out more and penetrate further in the spanwise direction into the passage for the flat endwall without blowing case as compared to the flat endwall with blowing.

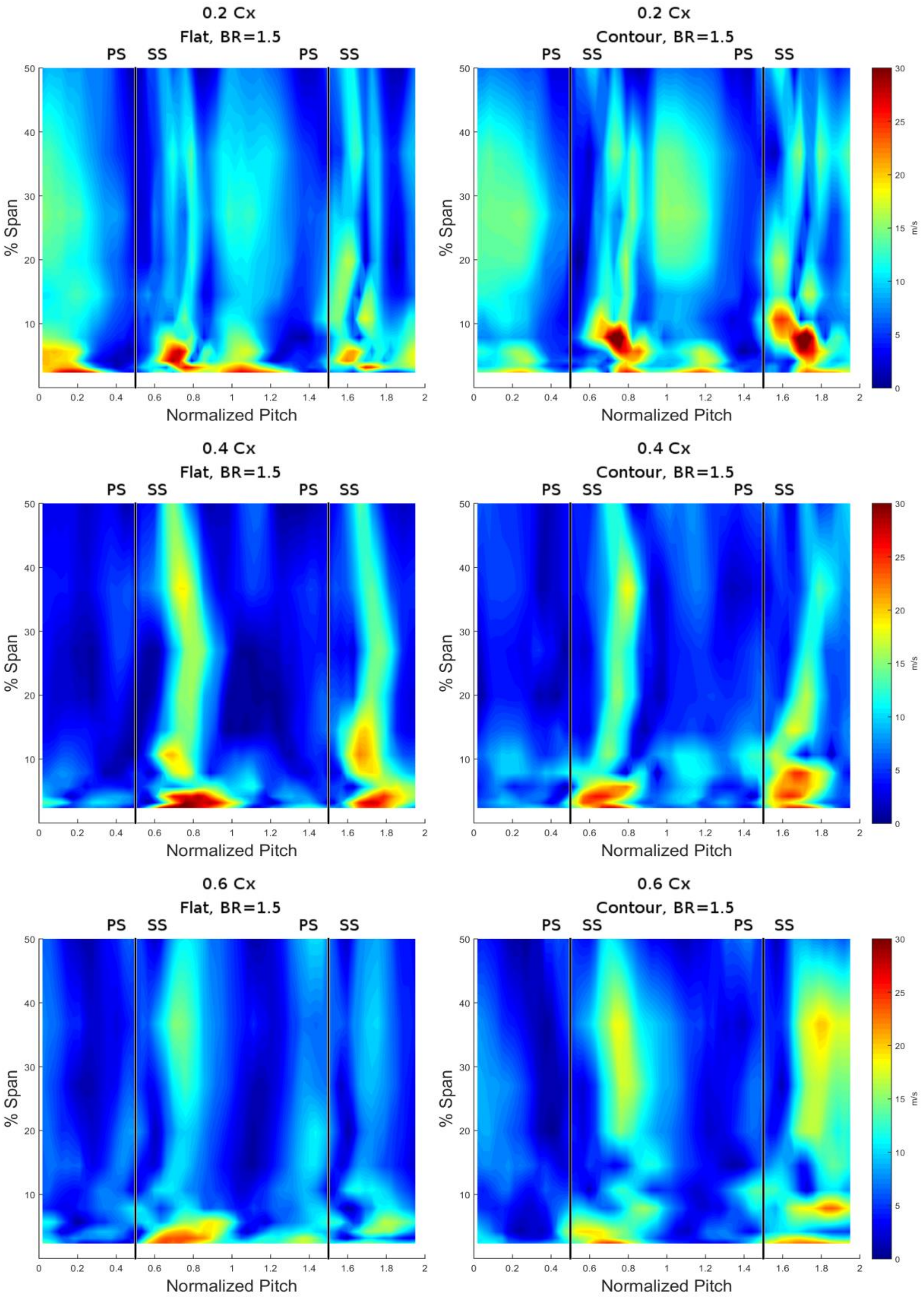

Figure 21. Secondary velocity magnitude for flat endwall (Left) and contoured endwall (Right) at 0.2 Cx (Top), 0.4 Cx (Middle), and, 0.6 Cx (Bottom)

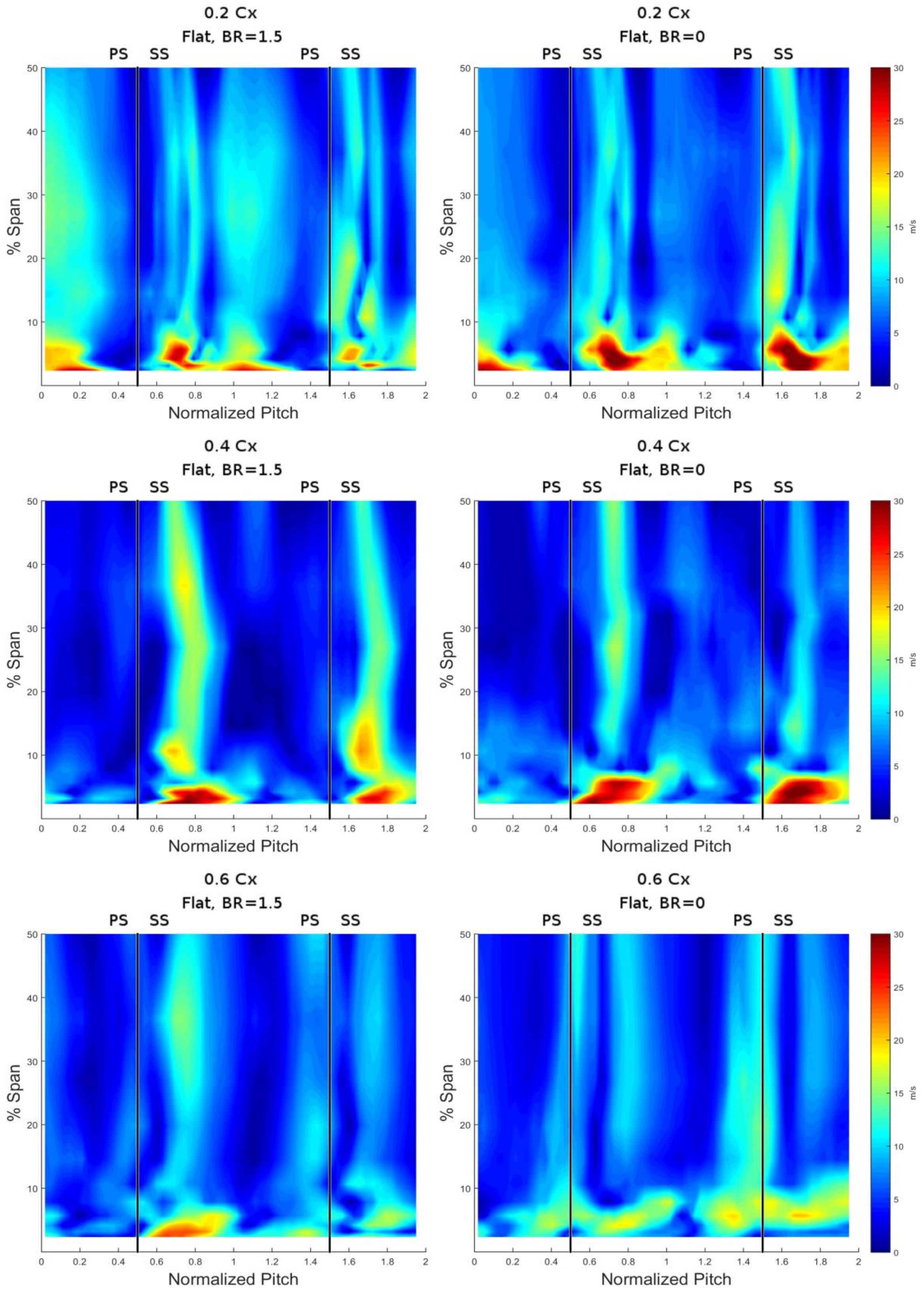
0.2 Cx Flat, BR=1.5

0.2 Cx Flat, BR=0

0.4 Cx Flat, BR=1.5

0.4 Cx Flat, BR=0

0.6 Cx Flat, BR=1.5

0.6 Cx Flat, BR=0

Figure 22. Secondary velocity magnitude for flat endwall (Left) and contoured endwall (Right) at 0.2 Cx (Top), 0.4 Cx (Middle), and, 0.6 Cx (Bottom)

4.3.4 Secondary Kinetic Energy

Secondary kinetic energy (SKE) is closely related to secondary velocity. The secondary velocity components at each point are squared and summed, and then the sum is normalized by the square of the primary velocity. As a result, SKE is a nondimensional result. Additionally, it should be noted that this squaring process results in weighing regions of peak loss more heavily than secondary velocity magnitude does. As a result, small regions with very high secondary velocities become comparatively more important than large regions with slightly elevated velocities. The calculation is shown by Equations 7 and 8.

$$SKE_i = \frac{\left(V_{sx}^2 + V_{sy}^2 + V_{sz}^2\right)_i}{\left|\overrightarrow{V_p}\right|_{mavg}^2} \tag{7}$$

$$\overrightarrow{V_p}_{mavg} = \frac{\sum\left(\dot{m}_i \overrightarrow{V_\iota}\right)}{\sum(\dot{m}_i)} \tag{8}$$

Figures 24 and 25 depict the results of this calculation for all exit planes. Figures 26 and 27 show the mass weighted spanwise averages for each exit plane.

Similar to the loss coefficient, there are identifiable peaks in the data at approximately 5% span corresponding to the passage vortex for most of the data. The literature [16] predicts these peaks, but it is not observed at all locations (namely, 0.2 Cx and 0.6 Cx for the flat endwall with blowing). This may be due to the high uncertainty from the probe measurements.

These peaks are generally lower and over a wider span for the contoured endwall than for the flat endwall, with the exception of at 0.2 Cx where the peak is higher for the contoured endwall. As expected, this loss core occurs farther from the endwall for the contoured case. SKE is higher near midspan for the contoured endwall case.

The flat endwall with blowing exhibits lower SKE than the flat endwall without blowing in the peak region near the passage vortex, but higher near midspan. Additionally, the passage vortex stays closer to the endwall, consistent with the results from loss coefficient and flow visualization.

Overall mass averaged values were calculated, and are tabulated in Table 5. None of the differences are outside of the uncertainties. While the contour does seem to improve SKE near the passage and counter vortices, it appears that this is not enough to offset increases in SKE near the wall and near midspan.

Table 4. Total mass averaged SKE for each case.

Mass Averaged SKE						
Axial Location (Cx DS)	0.2		0.4		0.6	
Contoured, BR=1.5	1.39E-03	±5.66E-04	8.13E-04	±5.62E-04	8.37E-04	±5.62E-04
Flat, BR=1.5	1.06E-03	±5.65E-04	6.73E-04	±5.56E-04	7.13E-04	±5.77E-04
Flat, No Blowing	1.05E-03	±5.66E-03	7.76E-04	±5.63E-04	8.52E-04	±5.63E-04

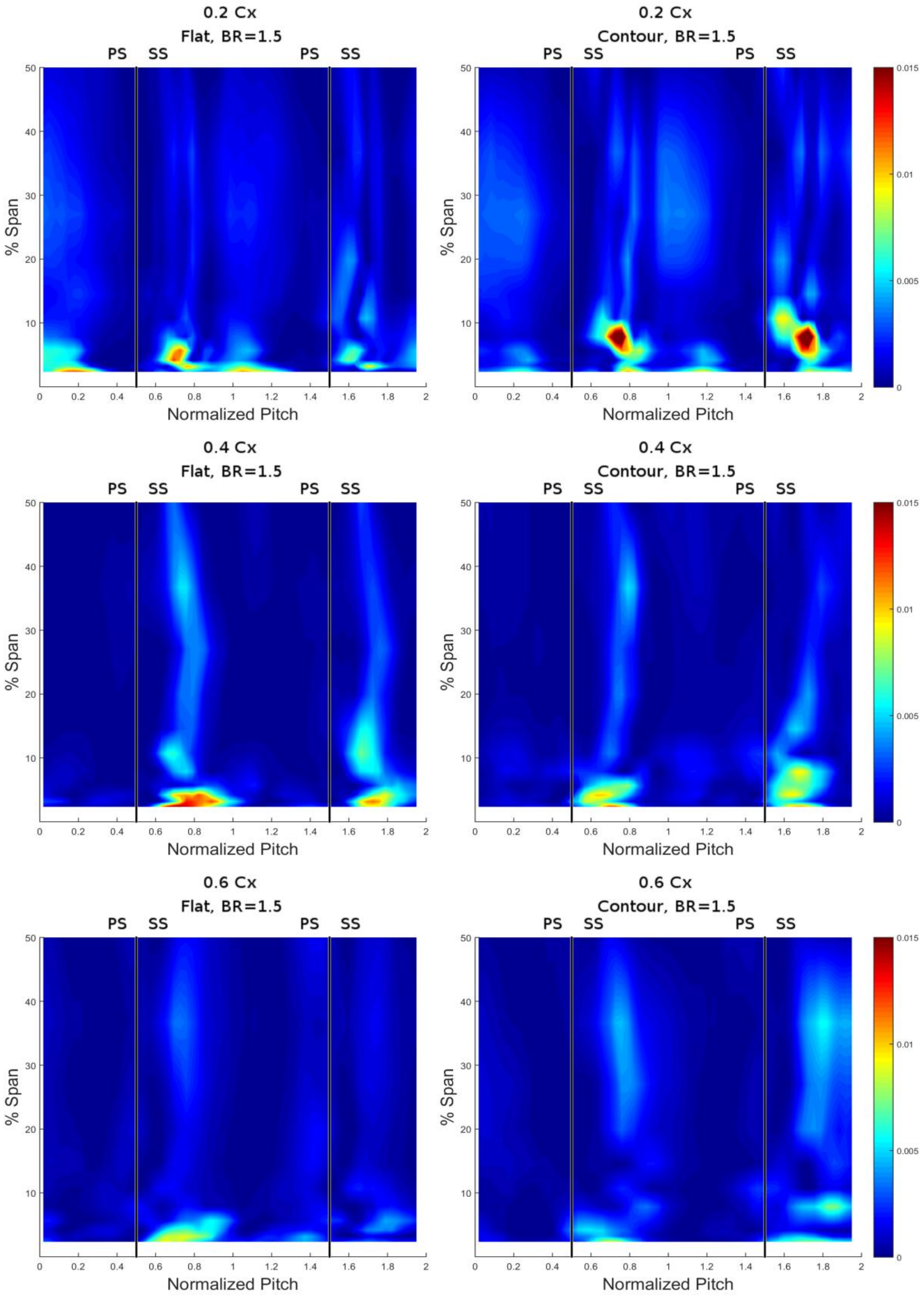

Figure 23. Secondary kinetic energy for flat endwall (Left) and contoured endwall (Right) at 0.2 Cx (Top), 0.4 Cx (Middle), and, 0.6 Cx (Bottom)

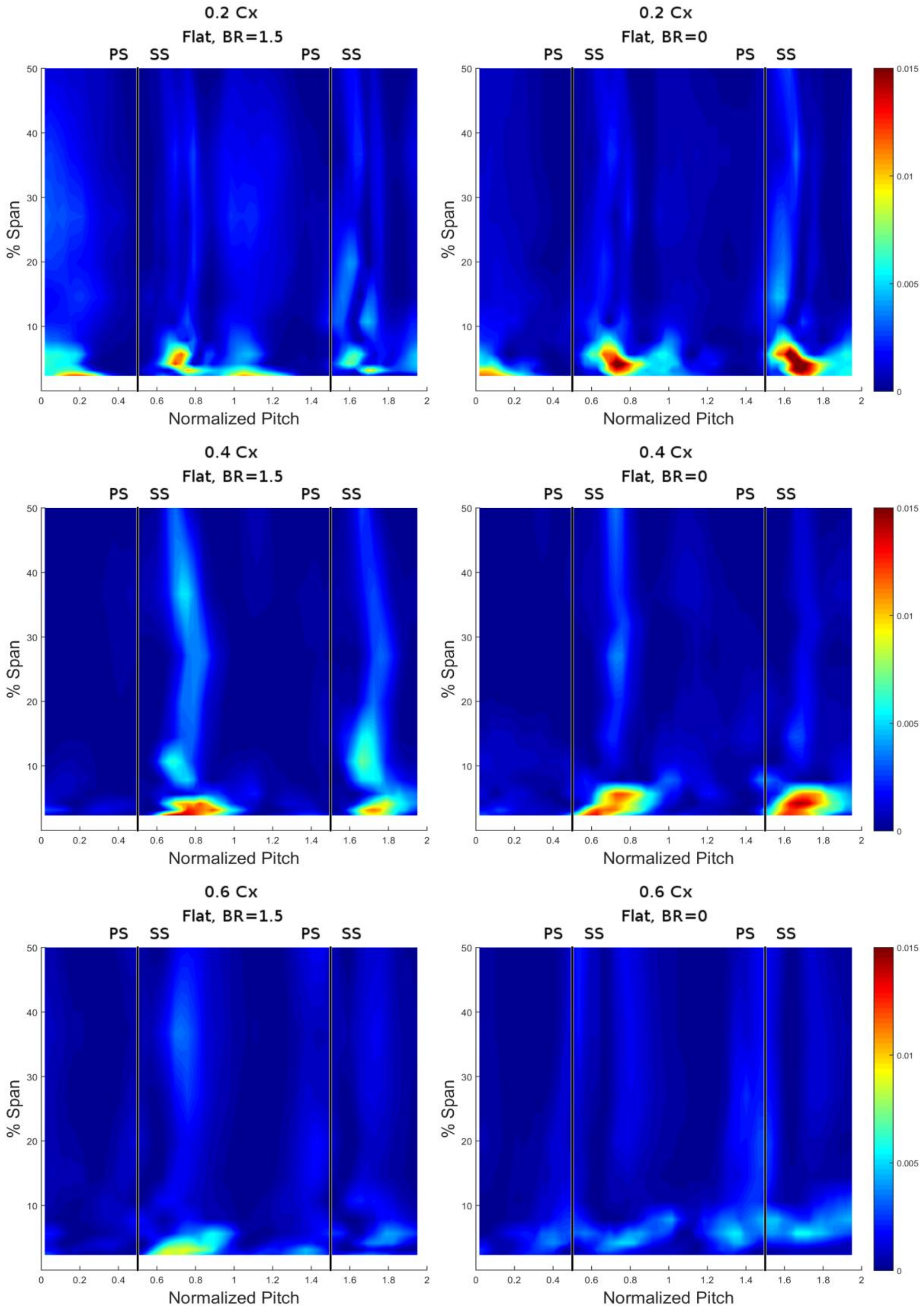

Figure 24. Secondary kinetic energy for flat endwall (Left) and contoured endwall (Right) at 0.2 Cx (Top), 0.4 Cx (Middle), and, 0.6 Cx (Bottom)

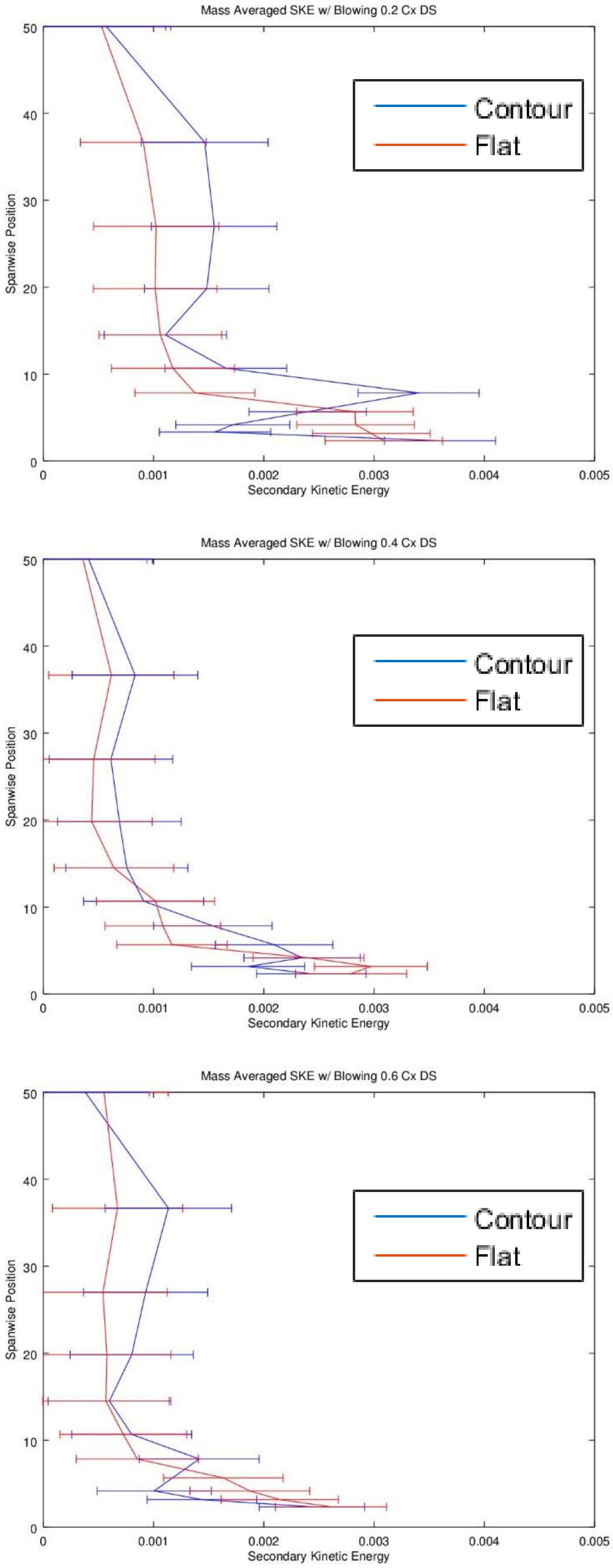

Figure 25. Mass averaged SKE plots for contoured and flat endwalls at 0.2 Cx (Top), 0.4 Cx (Middle), and 0.6 Cx (Bottom)

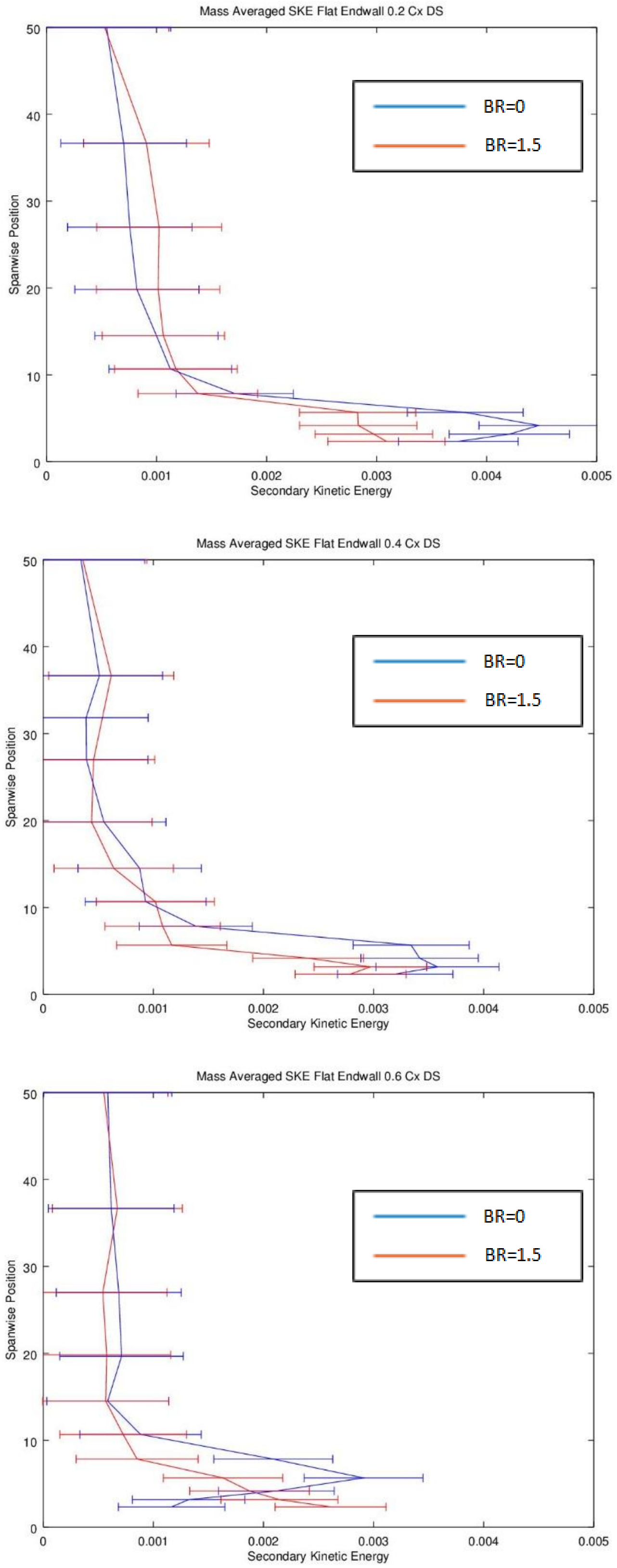

Figure 26. Mass averaged SKE plots for flat endwall with BR=0 and BR=1.5 at 0.2 Cx (Top), 0.4 Cx (Middle), and 0.6 Cx (Bottom)

5 Conclusions

Midspan static pressure taps match CFD well and have good periodicity, confirming that tunnel conditions are being met and that the vanes are functioning as expected. There is no significant difference in near-wall loading between contoured and flat endwalls, or between blowing and no blowing with a flat endwall.

Oil flow visualization shows that the passage vortex lifts off earlier for the contoured endwall case and penetrates further into the passage than for the flat endwall case. The passage vortex lifts off earlier, but remains closer to the endwall for the flat endwall with blowing, compared to the flat endwall without blowing. Less of the inlet boundary layer is entrained into the passage vortex flow in the contoured endwall case.

Loss coefficient, secondary velocity magnitude, and secondary kinetic energy measurements corroborate the flow visualization results by confirming that the passage vortex moves further into the passage for the contoured endwall compared to flat, and stays closer to the endwall for blowing compared to no blowing.

The expected flow features are observed in the downstream measurements (passage, counter, and corner vortices). The contoured endwall is observed to diffuse the passage and counter vortices, as expected by the existing literature.

No statistically significant difference in the overall mass averaged values for loss coefficient, secondary velocity magnitude, or secondary kinetic energy are observed. This may be due to the high uncertainty in the measurement, or there may not actually be any improvement from the contour. The passage vortex is weaker to begin with as compared to most existing literature due to the low turning, leaving a low margin for improvement. Additionally, the backward-facing step (which is not present in the other literature) makes the prediction of losses more difficult.

6 Recommendations for Future Work

Future work could improve upon this experiment in multiple ways. Additional measurement methods in order to reduce uncertainty may also be useful. Particle image velocimetry, if applied successfully, could potentially allow better measurement resolution and reduction in uncertainty.

Reducing the solidity of the cascade by increasing the spacing between airfoils would cause an increase in secondary flows and allow for more improvement. This would make it more likely to find differences that exceed the experimental uncertainty. Using a lower aspect ratio, unless precluded by a measurement technique such as PIV, may reduce the relative uncertainty by reducing the size of the area unaffected by the endwall.

The backward facing step may interact in a complicated way with the development of the leading edge horseshoe vortex. A method of analyzing this interaction may help understand its effect on the development of the secondary flow.

7 References

1. Denton, J.D., *The 1993 IGTI Scholar Lecture: Loss Mechanisms in Turbomachines.* Journal of Turbomachinery, 1993. **115**(4): p. 621-656.
2. Taremi, F., S.A. Sjolander, and T.J. Praisner. *Measurements of Endwall Flows in Transonic Linear Turbine Cascades: Part I - Low Flow Turning*. in *ASME Turbo Expo 2010: Power for Land, Sea, and Air*. 2010. American Society of Mechanical Engineers.
3. Wang, H.P., et al., *Flow Visualization in a Linear Turbine Cascade of High Performance Turbine Blades.* Journal of Turbomachinery, 1997. **119**(1): p. 1-8.
4. Langston, L., M. Nice, and R. Hooper, *Three-dimensional flow within a turbine cascade passage.* Journal of Engineering for Gas Turbines and Power, 1977. **99**(1): p. 21-28.
5. Langston, L., *Crossflows in a turbine cascade passage.* Journal of Engineering for Gas Turbines and Power, 1980. **102**(4): p. 866-874.
6. Gregory-Smith, D., *Secondary flows and losses in axial flow turbines.* Journal of Engineering for Gas Turbines and Power, 1982. **104**(4): p. 819-822.
7. Sieverding, C. and P. Van Den Bosche, *The use of coloured smoke to visualize secondary flows in a turbine-blade cascade.* Journal of Fluid Mechanics, 1983. **134**: p. 85-89.
8. Hartland, J., et al., *Nonaxisymmetric turbine end wall design: part II—experimental validation.* Journal of Turbomachinery, 2000. **122**(2): p. 286-293.
9. Chung, J. and T. Simon. *Effectiveness of the gas turbine endwall fences in secondary flow control at elevated freestream turbulence levels*. in *ASME, International Gas Turbine and Aeroengine Congress and Exposition, Cincinnati, OH*. 1993.
10. Aunapu, N.V., et al., *Secondary Flow Measurements in a Turbine Passage With Endwall Flow Modification.* Journal of Turbomachinery, 2000. **122**(4): p. 651-658.
11. Zess, G.A. and K.A. Thole, *Computational Design and Experimental Evaluation of Using a Leading Edge Fillet on a Gas Turbine Vane.* Journal of Turbomachinery, 2002. **124**(2): p. 167-175.
12. Germain, T., et al., *Improving Efficiency of a High Work Turbine Using Nonaxisymmetric Endwalls—Part I: Endwall Design and Performance.* Journal of Turbomachinery, 2010. **132**(2): p. 021007.
13. Knezevici, D., et al. *Measurements of Secondary Losses in a High-Lift Front-Loaded Turbine Cascade With the Implementation of Non-Axisymmetric Endwall Contouring*. in *ASME Turbo Expo 2009: Power for Land, Sea, and Air*. 2009. American Society of Mechanical Engineers.
14. Knezevici, D., et al., *Measurements of secondary losses in a turbine cascade with the implementation of nonaxisymmetric endwall contouring.* Journal of Turbomachinery, 2010. **132**(1): p. 011013.
15. Taremi, F., S.A. Sjolander, and T.J. Praisner, *Application of endwall contouring to transonic turbine cascades: Experimental Measurements at design conditions.* Journal of Turbomachinery, 2013. **135**(1): p. 011031.
16. Taremi, F., S. Sjolander, and T. Praisner. *Measurements of endwall flows in transonic linear turbine cascades: part II—high flow turning*. in *ASME Turbo Expo 2010: Power for Land, Sea, and Air*. 2010. American Society of Mechanical Engineers.
17. Jain, S., et al. *Aerodynamic Performance of a Transonic Turbine Blade Passage in Presence of Upstream Slot and Mateface Gap with Endwall Contouring*. in *ASME Turbo Expo 2014: Turbine Technical Conference and Exposition*. 2014. Düsseldorf, Germany: ASME.
18. Brennan, S., *Experimental Investigation of the Aerodynamics of a Turbine Nozzle Guide Vane with 3D Contoured Endwall Geometries.* Mechanical Engineering Master's Thesis, Virginia Polytechnic Institute and State University, 2014.

19. Peterson, K., *Experimental Investigation of the Aerodynamics of a Transonic Turbine Blade in a Cascade with 3D Contoured Endwall Geometries.* Mechanical Engineering Master's Thesis, Virginia Polytechnic Institute and State University, 2015.
20. Nguyen, B.Q., Honeywell Aerospace Internal Design Document.
21. Kline, S.J. and F. McClintock, *Describing uncertainties in single-sample experiments.* Mechanical engineering, 1953. **75**(1): p. 3-8.
22. Steele, H.W and W.G. Coleman, *Experimental Validation and Uncertainty Analysis for Engineers*. 2009: John Wiley & Sons, Inc.

Appendix

A General Tunnel Instrumentation

This section describes the instrumentation used to take pressure measurements for downstream data and surface loading, as well as experimental procedures done to improve the accuracy of the results.

A.1 Upstream Total and Static Pressure Measurements

Upstream pressure measurements were taken in the upper passages that were not used for downstream measurements. This was done in order to avoid any disturbances caused by the wake of the total pressure probes on the five-hole probe downstream. The reading from two probes was averaged in order to improve accuracy, as well as to detect any errors with the probe. If there was ever more than about a 1% difference between the two readings, it would be indicative of an issue with one of the probes.

In order to verify that the inlet profile was uniform enough to use the probes in the upper passage to estimate the pressure in the passages of interest, a test was performed with six total probes-the two that would be used during data collection, three in the passages of interest, and one in the lower passages. Less than 1% difference was found between these measurements, which was considered acceptable.

The two total pressure probes extended out to midspan of the upstream flow, and were located 1.4 Cx upstream of the vane leading edge. Four static pressure ports were also located upstream and were averaged. This allowed calculation of the upstream Mach number and velocity (needed to determine the blowing ratio).

A.2 Downstream Static Measurements

In order to measure the exit Mach number, downstream static pressure measurements were taken. Nine static wall taps were placed 0.9 Cx downstream of the trailing edge, and their pressures were averaged and used to determine the tunnel conditions. A larger number of taps were needed downstream because the five hole probe disturbs some of the taps as it moves pitchwise. For consistency, the Mach number for each run was calculated based off of the beginning of the run (before the traverse moved) and the upstream total pressure was monitored throughout the run to ensure a consistent Mach number. A constant (±0.1 psi) upstream total pressure was required for an acceptable run.

B Additional Vane and Endwall Details

Six vanes made up the test section, in order to create five passages. The vanes in the passages of interest were printed with a Fortus 250mc printer, using ABS. Fortus specifies a build layer thickness of 0.007 in and X/Y accuracy of ±0.0095 in. The vanes had threaded inserts attached to the side near the endwall in order to be securely bolted to the endwall and avoid leakage. Because a smooth surface finish was necessary for proper aerodynamic behavior, the vanes were prepared by very lightly sanding their surfaces and then painting on a thin layer of acetone. This results in a texture that is smooth to touch, unlike the material directly out of the printer.

A second set of central vanes was printed in order to take loading measurements. These were printed with holes at 4% span, and were instrumented with brass tubes that were connected to the pressure system during runs.

The flat endwall was printed on the same Fortus printer as the vanes, in three pieces designed to have two vanes each. Additionally, the vanes for the upper and lower doublets were printed as a single piece with the endwall, eliminating any concerns of leakage at those points. The central doublet used separate vanes that bolted on for consistency with the contoured endwall and reusability with the loading vanes. Figure 28 shows how this setup works. The holes for loading measurements are visible near the endwall.

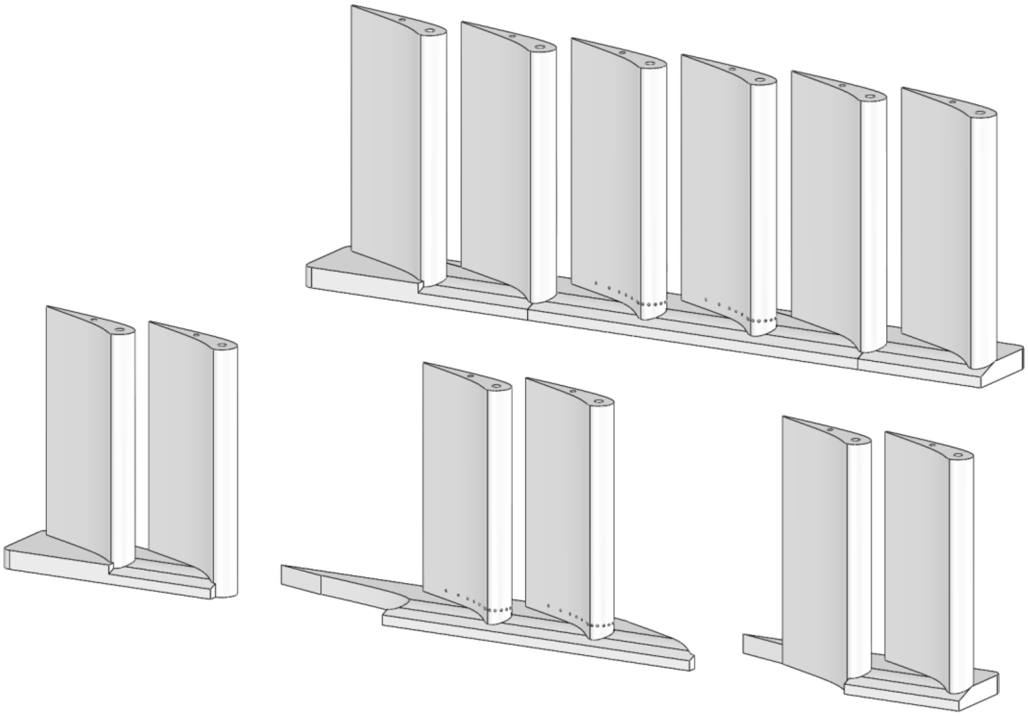

Figure 27. Flat endwall configuration as three pieces. Central piece has removable vanes

The contoured endwall was printed on a Stratasys Connex3 3D printer, using an ABS-like material. The build layer for the Connex3 is 0.0006 inches and the X/Y accuracy is ±0.0017 inches. It was printed as a single piece. It was prepared in the same way as the vanes, by sanding and then applying acetone. Six independent vanes were used and attached to the endwall. Figure 29 shows the contoured endwall.

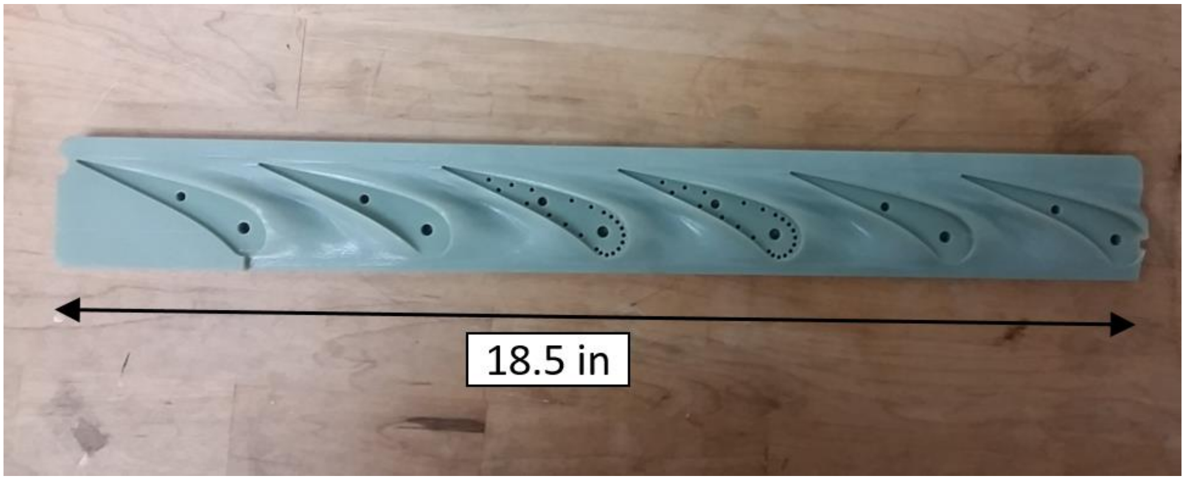

Figure 28. Contoured endwall. Vanes are bolted individually to each of the cutouts in the endwall

C Additional Purge Flow Details

In order to supply the upstream purge flow, an external plenum was designed to mate externally to the window. This formed a cavity between the plenum and the upstream step (which has the purge flow holes drilled into it). Air is supplied to this cavity from both sides for symmetric airflow, and a thermocouple is inside in order to monitor the temperature. Gaskets are used for both the plenum and the upstream step to avoid leakage. Figure 30 shows the plenum, and Figure 31 shows the flow path of air moving through the plenum to the purge flow holes.

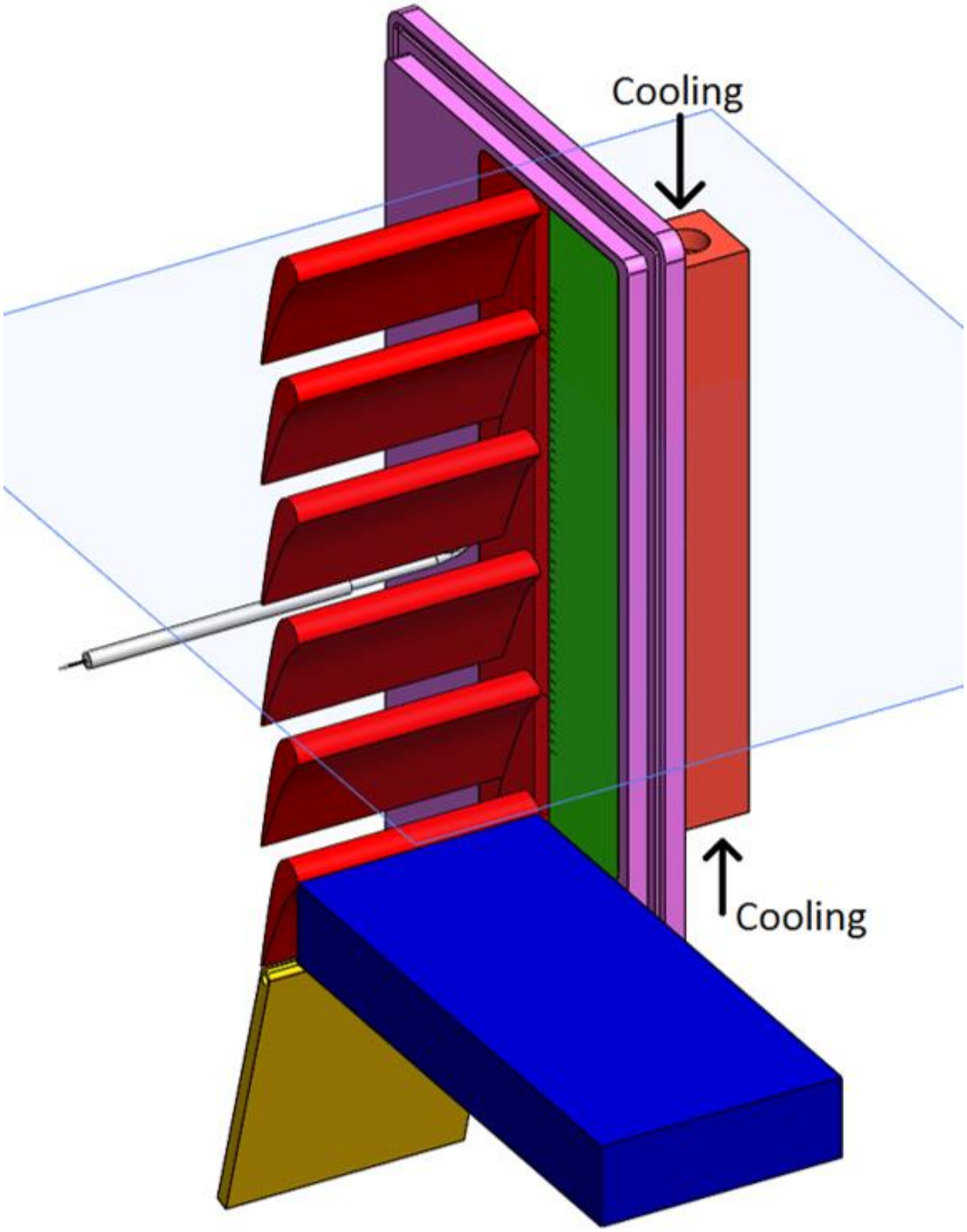

Figure 29. View of external plenum. Cooling supplied to both sides simultaneously

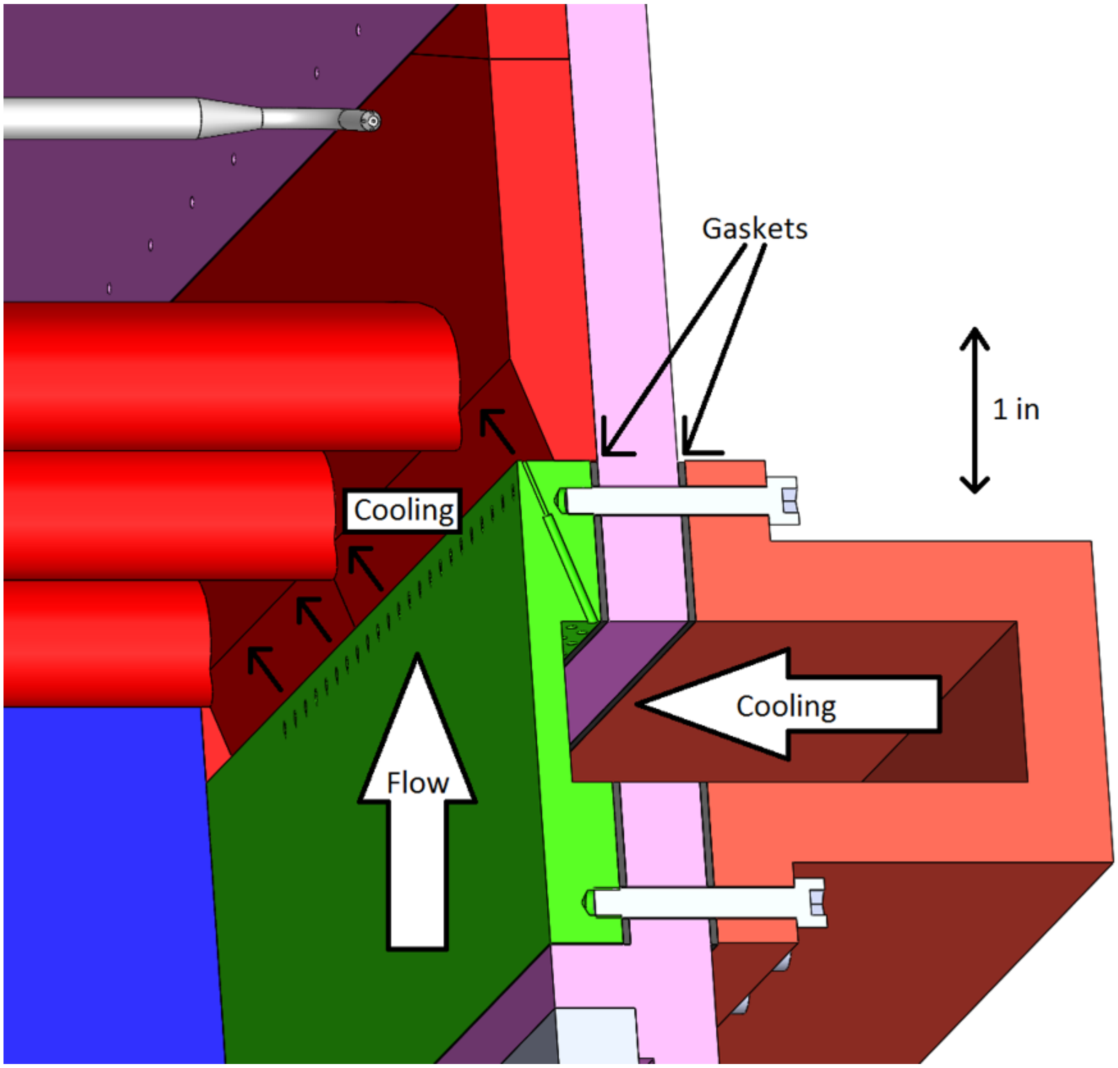

Figure 30. Flow of purge flow air through the plenum and into the test section

The holes in the upstream step are a larger diameter initially in order to reduce losses, and are the designed 0.055 inch diameter for the final ½ inch of length. This hole diameter was chosen to match the engine mass flow ratio when the blowing ratio is set to the desired value of 1.5. The air for the purge flow is supplied from an external tank, which is connected through a series of pipes. An orifice mass flow meter was used to determine the mass flow rate for the purge flow and therefore calculate the blowing ratio. The blowing ratio is calculated by the following formula:

$$BR = \frac{\rho_c U_c}{\rho_\infty U_\infty} = \frac{m_c / A_c}{\rho_\infty U_\infty}$$

The total area of the coolant holes is known from the geometry, and the upstream density and velocity are determined using the upstream pressure taps and thermocouple. As a result, the blowing ratio can be determined from the purge flow mass flow rate. The blowing ratio was set to be 1.5 ± 0.05.

D Traverse Setup Details

There were multiple interfaces in the hardware, especially between the endwall and the window. This was necessary in order to reuse the same window for each configuration. In order to avoid errors from gaps or steps at these interfaces, JB-Weld was used to fill the gaps and surrounding area. It was then sanded to make a smooth interface from the endwall to the window. Figure 32 shows this JB-Weld, prior to a flow visualization run.

Figure 31. Smooth interface between window and endwall

An airtight traverse box was mounted to the window to avoid leakage out the traverse slot. The box contains all the hardware needed to traverse the probe pitchwise during a run, using a Velmex traverse with a stepper motor. It also contains a second, manual traverse, which is used to adjust the spanwise position in between runs.

E Five-hole Probe Details

The probe was held at the exit flow angle of the vane row by the traverse box. This angle was set once, before taking any data, and was checked periodically. For each exit plane, it was held at a constant axial distance downstream of the leading edge. For every run within the exit plane, the probe was set to the necessary spanwise position using the manual axis of the traverse box, and traversed pitchwise at 1 inch per second through the passages of interest. This speed was tested by Peterson [19] to ensure that it was slow enough to accurately capture the flow. 11 spanwise locations were sampled, logarithmically spaced from 2.3% span (0.14 inches) to 50% span (3 inches). All measurements were taken in the half of the test section closest to the endwall, requiring the probe to cantilever across 3 or more inches of the test section. An additional spanwise measurement was taken at 1.6% span but was not reported (the probe is calibrated in a free stream and cannot be relied on for accuracy that closely to the wall).

Additional specifications for the probe are below.

- Manufacturer: Aeroprobe Corporation
- Calibration data base provided by Aeroprobe, used with interpolation
- Calibration provided for a range of Mach numbers from 0.4 to 1.2
- Measurement variables and specified accuracies:
    - Velocity components (u, v, w) (accuracy ±0.4%)
    - Flow angles (pitchwise and spanwise) (accuracy ±0.4°)
    - Total pressure and static pressure
- Maximum flow angle deviation from tip axis
    - Subsonic (pitchwise ±60° and spanwise ±60°)
    - Supersonic (pitchwise ±30° and spanwise ±30°)
- Probe tip dimensions
    - 0.125 in diameter
    - 1.000 in length
- Bending Analysis (at Mach 1.2):
    - Maximum deflection: 1.0mm;
    - Max slope: 0.2 degree.

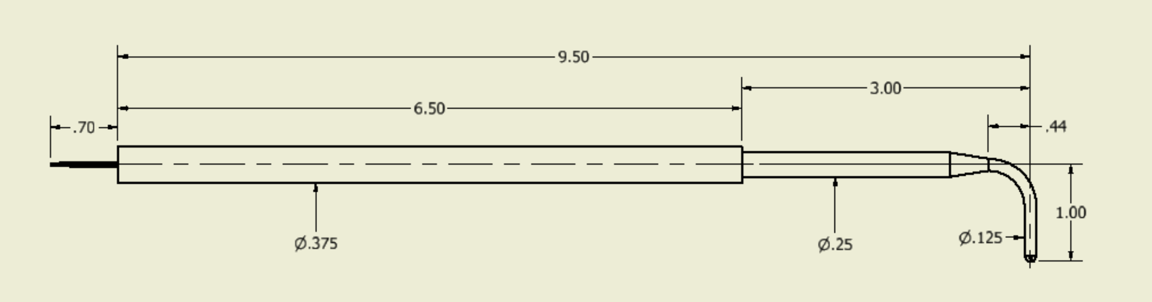

Figure 32. Five-hole probe dimensions

F Repeatability

Repeatability from run to run and day to day was established by comparing the raw probe data taken from separate runs at the same location on different days. This helps establish that tunnel conditions are being reached reliably, among other potential errors. The P1 pressure (pressure from the hole at the tip of the probe) was used for this comparison. The results from one set of repeatability runs are below in Figure 34.

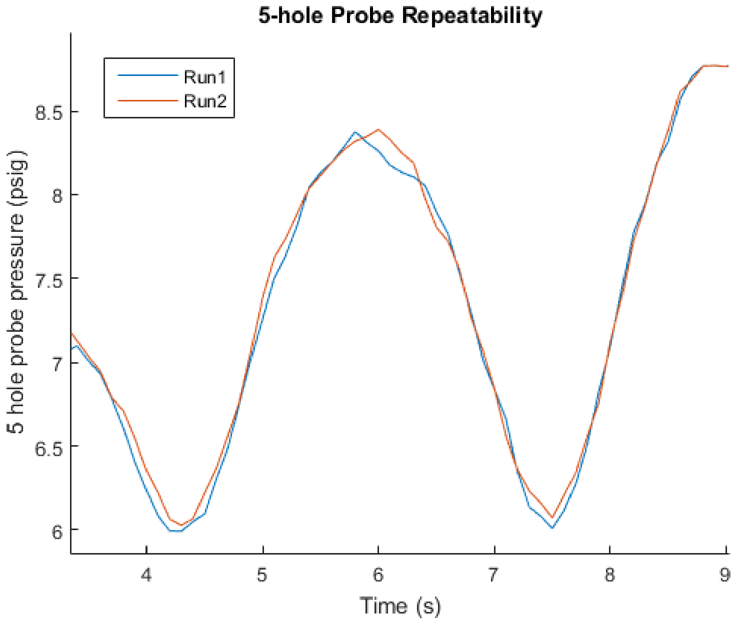

Figure 33. Five-hole probe data collected from two separate days (same test setup and spanwise location)

G Uncertainty Analysis

An uncertainty analysis was performed in order to quantify the measurement error and determine whether results were statistically significant or not. Manufacturer uncertainties were used for all of the equipment, and are listed below.

- Five-hole probe velocity component accuracy: ±0.4%
- Five-hole probe flow angle accuracy: ±0.4°
- Pressure measurement accuracy: ±0.05%
- Thermocouple accuracy: ±0.4%

For loss coefficient, the uncertainty analysis used the same method as Peterson [19], which in turn utilized Kline and McClintock's method for calculating experimental uncertainty [21]. Analysis for the loss coefficient is straightforward because it is fundamentally a local quantity, and is independent of measurements at other points.

In previous experiments (Brennan [18], Peterson [19]) a large portion of the uncertainty came from the alignment of the five hole probe. Peterson estimated this uncertainty as ±0.25° in pitch and ±0.50° in yaw, leading to approximately double the overall uncertainty in flow angle overall. However, for this experiment, the new traverse box allowed motion in both the pitchwise and spanwise directions without ever removing the probe. As secondary velocities (and consequently derived quantities such as SKE) are defined as relative rather than absolute, this effectively subtracts off the error in probe alignment, leaving only the accuracy of the probe itself.

Additionally, a different method of calculating uncertainties was implemented. Errors were propagated using a Taylor Series Method, as defined by Coleman and Steele [22]. They give two formulas for error propagation for combining uncertainties from multiple sources. For a result r that is a function of independent measurements X_i, for i from 1 to J:

$$u_r^2 = \sum_{i=1}^{J} \left(\frac{\partial r}{\partial X_i}\right)^2 b_{X_i}^2 + \sum_{i=1}^{J} \left(\frac{\partial r}{\partial X_i}\right)^2 s_{X_i}^2$$

Where b_{X_i} and s_{X_i} are respectively the systematic (sometimes also called bias) and random uncertainties of the measurements X_i.From Section 8.6 (Repeatability) it is clear that random errors (variations from run to run under the same condition) are small. Furthermore, many data points are taken (732 per plane). It is therefore expected that random, independent errors (errors between identical runs at the same data point) will largely offset each other. Systematic errors, however, will not offset each other, and are the main component of the experimental uncertainty.

Considering only systematic errors, we get:

$$u_r^2 = \sum_{i=1}^{J} \left(\frac{\partial r}{\partial X_i}\right)^2 b_{X_i}^2$$

As an example, for a result dependent on two measurements X_1 and X_2, each with systematic uncertainties b (the uncertainties are equal, but the errors are independent from each other), this reduces to:

$$u_r^2 = \left(\frac{\partial r}{\partial X_1}\right)^2 b^2 + \left(\frac{\partial r}{\partial X_2}\right)^2 b^2 = b^2 \left[\left(\frac{\partial r}{\partial X_1}\right)^2 + \left(\frac{\partial r}{\partial X_2}\right)^2\right]$$

$$u_r = b\sqrt{\left[\left(\frac{\partial r}{\partial X_1}\right)^2 + \left(\frac{\partial r}{\partial X_2}\right)^2\right]}$$

If furthermore, $\left(\frac{\partial r}{\partial X_1}\right) = \left(\frac{\partial r}{\partial X_2}\right)$, as in the equation $u_r = 3(X_1 + X_2)$, we have:

$$u_r = \sqrt{2}\, b \left(\frac{\partial r}{\partial X_1}\right)$$

The other equation that is given by Coleman and Steele accounts for correlated error terms by using covariances. For systematic errors only, the equation for a result dependent on X_1 and X_2 is:

$$u_r^2 = \left(\frac{\partial r}{\partial X_1}\right)^2 b_{X_1}^2 + \left(\frac{\partial r}{\partial X_2}\right)^2 b_{X_2}^2 + 2\left(\frac{\partial r}{\partial X_1}\right)\left(\frac{\partial r}{\partial X_2}\right) b_{12}$$

$$b_{12} = \sum_{\alpha=1}^{L} (b_{i_\alpha})(b_{j_\alpha})$$

Where L is the number of systematic error sources shared by X_1 and X_2. Repeating the same process for as for the system with independent systematic errors, but this time with errors that always identical:

$$b_{12} = b * b = b^2$$

$$u_r^2 = \left(\frac{\partial r}{\partial X_1}\right)^2 b^2 + \left(\frac{\partial r}{\partial X_2}\right)^2 b^2 + 2\left(\frac{\partial r}{\partial X_1}\right)\left(\frac{\partial r}{\partial X_2}\right) b^2$$

$$u_r^2 = b^2\left[\left(\frac{\partial r}{\partial X_1}\right)^2 + \left(\frac{\partial r}{\partial X_2}\right)^2 + 2\left(\frac{\partial r}{\partial X_1}\right)\left(\frac{\partial r}{\partial X_2}\right)\right]$$

$$u_r^2 = b^2\left[\left(\frac{\partial r}{\partial X_1}\right) + \left(\frac{\partial r}{\partial X_2}\right)\right]^2$$

$$u_r = b\left[\left(\frac{\partial r}{\partial X_1}\right) + \left(\frac{\partial r}{\partial X_2}\right)\right]$$

For $\left(\frac{\partial r}{\partial X_1}\right) = \left(\frac{\partial r}{\partial X_2}\right)$, we get:

$$u_r = 2b\left(\frac{\partial r}{\partial X_1}\right)$$

Which is larger than the result obtained for the uncorrelated errors. In general, if the partial derivatives of the result relative to the measurement are the same sign, positively correlated errors will result in greater uncertainty in the result than uncorrelated or negatively correlated errors.

The analysis for more complicated systems proceeds analogously. For example, in calculating primary velocity, the measurements at each data point may reasonably be assumed to share a systematic error in the probe measurement. The calculation for the x component of primary velocity is:

$$V_{x_{mavg}} = \frac{\sum(\dot{m}_i V_{x_i})}{\sum(\dot{m}_i)}$$

If each velocity V_{x_i} has an uncertainty $B_{V_{x_i}}$, the uncertainty calculation becomes:

$$B_{V_{p_x}} = \frac{\sum\left(\dot{m}_i B_{V_{x_i}}\right)}{\sum(\dot{m}_i)}$$

It is important to realize that the classification of errors into systematic and random errors is dependent on the context. Coleman and Steele give the example of reading a set of voltages with the same multimeter. The calibration error of the multimeter in this context represents a systematic uncertainty (it applies equally to all measurements). However, this error itself follows a statistical distribution, representing the calibration errors of all multimeters of this particular model.

In this case, there are many potential levels of systematic and random errors. An error could be systematically correlated for a certain subset of measurements, but random within the greater context of the experiment. In summary, an error can be:

1. Random from data point to data point within a run
    - Electrical noise, for example
2. Systematic over the course of a single run, but random from run to run at the same location
    - Would include errors in tunnel conditions (Mach number was maintained very closely)
3. Systematic within a certain spanwise location, but random between different locations
    - Errors in probe alignment and probe accuracy likely fall into this category
4. Systematic for a single setup, but random between setups
    - Misalignment of traverse box that stays constant for a plane of data

The large number of data points renders errors of category 1 negligible, while the relative nature of SKE calculations makes many errors of category 4 mostly irrelevant. The repeatability study in Section 8.6 shows that errors of category 2 are small. Therefore, errors of category 3 are the most damaging. This is consistent with the observations of Peterson [19], who observed most of his uncertainty depended on the alignment of the probe.

Additionally, there exists the possibility of errors that are systematic for a single setup (category 4), but affect measurements at different regions of the flow differently and therefore are not subtracted off in the calculation of secondary velocity. These errors are likely the hardest to evaluate correctly.

Combining all of this information, it is possible to calculate a reasonable estimate of the uncertainty in SKE based on the uncertainties in local velocity, which has been reported here.

The fundamental problem in measuring secondary velocity to a high degree of certainty is the small magnitude of the secondary flow relative to the main flow. As a result, small magnitude errors in measuring the main flow are approximately the same size as the true secondary flow. Even though the velocity components measured by the five-hole probe are accurate to ±0.4%, the uncertainty of the final reduced result (SKE) is closer to ±50%.

Future research would benefit by studying flows with greater secondary velocity magnitudes (for example, cascades with higher blade loading), as this would make it easier to measure. Alternatively, the accuracy in velocity measurements would need to be improved, but improving it to a point that SKE is measured accurately enough to draw quantitative conclusions might not be possible with current technology.

H Leakage Discussion

Leakage between the vane and endwall was a concern, due to issues with this during previous projects in the same facility. Leakage would lead to inaccurate downstream measurements. Silicone was used to create a gasket below the vanes, and they were securely bolted to the endwall to clamp this gasket. Tests were performed with leak detector to verify that there were no leaks prior to installation, and flow visualization tests provided an opportunity to check that no leaks had developed prior to removal of the vanes.

After performing flow visualization tests on each configuration, the vanes were removed and the mating surface with the endwall was checked for leakage. If any leakage had occurred, there would be streaks of flow visualization oil on this surface. None were found during any of the tests, verifying that there were no leaks. Figure 35 shows the surfaces left by the vanes after blowdown with flow visualization oils. As can be seen, there are no streaks of oil across the vane cutout.

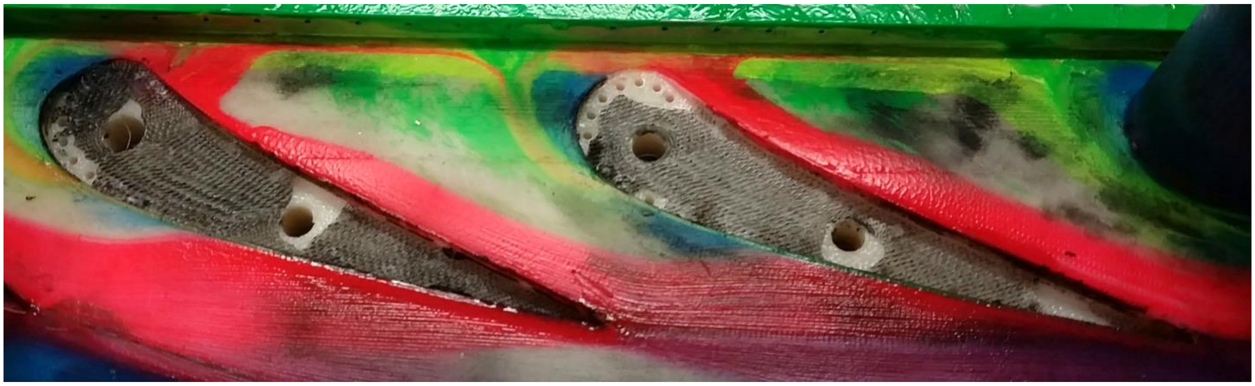

Figure 34. Verification that there is no leakage underneath the vane (underside of vane is also checked)